Lithology and Internal Structure of the San Andreas Fault at depth based on characterization of Phase 3 whole-rock core in the San Andreas Fault Observatory at Depth (SAFOD) Borehole

By Kelly K. Bradbury[1], James P. Evans[1], Judith S. Chester[2], Frederick M. Chester[2], and David L. Kirschner[3]
[1]Geology Department, Utah State University, Logan, UT 84321-4505
[2]Center for Tectonophysics and Department of Geology and Geophysics, Texas A&M University, College Station, Texas 77843
[3]Department of Earth and Atmospheric Sciences, St. Louis University, St. Louis, Missouri 63108

Abstract

We characterize the lithology and structure of the spot core obtained in 2007 during Phase 3 drilling of the San Andreas Fault Observatory at Depth (SAFOD) in order to determine the composition, structure, and deformation processes of the fault zone at 3 km depth where creep and microseismicity occur. A total of approximately 41 m of spot core was taken from three separate sections of the borehole; the core samples consist of fractured arkosic sandstones and shale west of the SAF zone (Pacific Plate) and sheared fine-grained sedimentary rocks, ultrafine black fault-related rocks, and phyllosilicate-rich fault gouge within the fault zone (North American Plate). The fault zone at SAFOD consists of a broad zone of variably damaged rock containing localized zones of highly concentrated shear that often juxtapose distinct protoliths. Two zones of serpentinite-bearing clay gouge, each meters-thick, occur at the two locations of aseismic creep identified in the borehole on the basis of casing deformation. The gouge primarily is comprised of Mg-rich clays, serpentinite (lizardite ± chrysotile) with notable increases in magnetite, and Ni-Cr-oxides/hydroxides relative to the surrounding host rock. The rocks surrounding the two creeping gouge zones display a range of deformation including fractured protolith, block-in-matrix, and foliated cataclasite structure. The blocks and clasts predominately consist of sandstone and siltstone embedded in a clay-rich matrix that displays a penetrative scaly fabric. Mineral alteration, veins and fracture-surface coatings are present throughout the core, and reflect a long history of syn-deformation, fluid-rock reaction that contributes to the low-strength and creep in the meters-thick gouge zones.

1. Introduction

The composition, texture, and internal structure of fault zones reveal how slip is accommodated during faulting and reflect the potential role of fluids during fault zone evolution (e.g. Chester and Logan, 1986; Evans, 1990; Chester et al., 1993; Knipe et al., 1993; Evans and Chester, 1995; Caine et al., 1996; Evans et al., 1997; Vrolijk and van der Pluijm, 1999; Faulkner et al., 2003; Wibberley et al., 2008). Though much of our understanding of active faulting in the continental crust is derived from examination of inactive, exhumed faults, it is clear that the composition and structure of these rocks may be modified during uplift and exhumation. Therefore to clarify fault structure and the physical and chemical processes of deformation at depth, it is critical to compare the results of the surface studies to research on samples obtained by drilling into active, large-displacement fault zones (Ohtani et al., 2000; Hickman et al., 2004; Reches and Ito, 2007; Tobin et al., 2007). Defining fault zone characteristics using core recovered by drilling is challenging because of the limited sample size, poor core retrieval, and potentially complex subsurface geology, especially in large displacement faults. Core-based studies, however, reduce the impact of exhumation-related overprinting that can obscure fault rock textures and geochemical signatures, and help reduce the uncertainty associated with using exhumed fault zones as a proxy for the analysis of *in situ* processes and mechanical behavior of active faults (e.g., Ohtani et al., 2000; Isaacs et al., 2007).

The San Andreas Fault Observatory at Depth (SAFOD) borehole near Parkfield, CA (Fig. 1) transects the San Andreas Fault (SAF) at approximately 3 km depth where aseismic creep occurs just 10's to 100's of meters up-dip from a region of persistent micro-earthquake activity (Hickman et al., 2004; 2007; Ellsworth et al., 2005; Thurber et al., 2004; 2006; Zoback et al., 2010). Numerous workers have hypothesized that the aseismic creeping behavior and low strength of the SAF in this region are related to the presence of key minerals and specific fluid-rock reaction processes (e.g. Allen, 1967; Irwin and Barnes, 1975; Wallace, 1990; Moore et al., 1996; Scholz, 2002; Hickman et al., 2004; Schleicher et al., 2006; 2009; 2010; Solum et al., 2006; Moore and Rymer, 2007; Tembe et al., 2006; 2009; Carpenter et al., 2009; 2011; Holdsworth et al., 2011; Janssen et al., 2010; Lockner et al., 2011; Mittempergher et al., 2011). In this paper, we add to the existing data set by systematically describing the rock units captured by coring and providing petrographic and geochemical analyses of 30 whole-rock samples to help constrain deformation processes and fluid-rock reactions within the near-fault environment.

1.1. Geologic Setting

The SAFOD borehole is in the central California Coast Ranges southwest of the surface trace of the SAF and north of the town of Parkfield, CA (Fig. 1a). This area lies within a transitional zone between the central creeping segment and the segments of the SAF that produce great earthquakes (Allen, 1968; Unsworth et al., 1997; Hickman et al., 2004; Rymer et al., 2006). Direct measurements indicate the fault creeps 2 to 3 cm/yr (Titus et al., 2005; 2006) with most deformation concentrated in a 10-m wide zone at the surface (Hickman et al., 2004). Aseismic creep and microseismicity at SAFOD occurs between 2.5 to 12 km depth (Thurber et al., 2006). Historical ruptures on the Parkfield segment, with M_w of approximately 6.0, including the M_w 6.0 earthquake in 2004, have occurred approximately 10 km south of the SAFOD location (Fig. 1; Harris and Arrowsmith, 2006).

Rocks exposed east of the SAF near SAFOD include folded and faulted Tertiary through Jurassic siliciclastic rocks, mélange of the Jurassic Franciscan Formation, and sheared serpentinite (Bailey et al., 1964; Dickinson, 1966; Dibblee, 1971; Sims, 1990; Page et al., 1998; Rymer et al., 2004; Thayer and Arrowsmith, 2006). Tertiary sedimentary rocks and Mesozoic Salinian granitoids are exposed to the west of the drill site (Dibblee, 1973; Sims, 1990). Prior to SAFOD drilling, geophysical studies attributed a shallow, high P-wave velocity region southwest of the SAF to Salinian granitoids and a distinct low-velocity region northeast of the SAF to the Franciscan Formation (Unsworth et al., 1997; McPhee et al., 2004; Thurber et al., 2004; Unsworth and Bedrosian, 2004; Zhang and Thurber, 2005; Hole et al., 2006).

1.2 SAFOD Borehole and Sampling

The SAFOD borehole was drilled approximately 1.8 km west of the surface trace of the SAF on the Pacific Plate and extends vertically downward to approximately 1.5 km, then is deviated at an angle of approximately 55° from vertical and trends northeastward (Fig. 1b). Herein we report depths along the borehole in meters measured depth (m MD) to represent the distance below the drill rig floor (http://www.earthscope/org/data/safod). The borehole crosses the active SAF and penetrates the North American Plate reaching a total measured depth of 3.9 km (Hickman et al., 2007). Borehole observations indicate that the nearest earthquake clusters are located within 100 m, and are directly below the borehole trajectory (Fig. 1c; Zoback et al., 2010). The location and distribution of earthquakes over the broader region is characterized by a complex pattern of seismicity consistent with the presence of multiple active slip surfaces in the shallow crust at SAFOD (Thurber et al., 2010).

Bradbury et al. (2007) identified the presence of Salinian granitic rocks in the SAFOD borehole based on cuttings retrieved during Phase 1 drilling between 760 and 1920 m MD. A deformed fault-bounded block of Paleocene-Eocene arkosic sedimentary rocks is juxtaposed with the eastern side of the Salinian block along the Buzzard Canyon fault (BCF) and extends eastward to the SAF zone (Fig. 1b; Hole et al., 2006; Springer et al., 2009). Geophysical data, and cuttings composed of abundant fragments of cataclasite, calcite veins, fine-grained sheared lithics, and flakes of serpentinite, suggest that this block is cut by multiple faults between 1920 and 3300 m MD. Juxtaposition of granite and sedimentary rocks is consistent with significant slip on the BCF, and Springer et al. (2009) suggest that the fault strands within the fault-bounded block also may have accommodated considerable displacement. Farther downhole, on the northeast side of the SAF, well-indurated siltstones and mudstones of the uppermost Cretaceous Great Valley sequence were identified in cuttings and Phase 2 spot core recovered from the easternmost end of the borehole (Bradbury et al., 2007; Pares et al., 2008; Springer et al., 2009).

Sidetrack drilling off of the main hole during Phase 3 intersected the SAF zone at a relatively high angle (Fig. 1c). From the sidetrack holes, approximately 41 m of 10 cm diameter, whole-rock core was successfully retrieved (Figs. 1-2) from three continuous intervals between 3141.4 and 3312.7 m MD. The intervals are referenced by hole and core run, i.e., Runs 1-3 in Hole E, Runs 1-3 in Hole G, and Runs 4-6 in Hole G. The Phase 3 core was cut at the drill site into sections 15 to 90 cm long. The depths of specific features captured in the Phase 3 core are slightly different than the depths of correlative features determined from the geophysical logs taken in the main hole (refer to Zoback et al., 2010 for detailed discussion).

A zone of low seismic velocity (LVZ, Fig. 1c) was indentified from the geophysical logs of the main borehole drilled in Phase 2. The interval between 3192 and 3413 m MD displays V_p and V_s values that are 10 to 30% lower than those for rocks to the east and west (Fig. 1d). This zone has relatively high porosity and is cut by multiple slip planes (Boness and Zoback, 2006; Li et al., 2004; Li and Malin, 2008; Zoback et al., 2010; Jeppson et al., 2010). Zoback et al. (2010) interpret this 200-m wide zone of reduced seismic velocity and resistivity as a fault-related damage zone of the currently active SAF. Deformation within the granitic rocks and arkosic sandstones west of the SAF suggest a thicker overall damage zone that reflects multiple episodes of movement along relict and active faults (Chester et al., 2010). Pronounced casing deformation, caused by fault creep, occurs at two localities that are characterized by anomalously low V_p, V_s, and resistivity, and low total natural gamma signatures. The two regions of fault creep are referred to as the Southwest Deforming Zone (SDZ), located at 3192 m MD, and the Central Deforming Zone (CDZ), located at 3302 m MD (Fig. 1d; Zoback et al., 2010). The SDZ and CDZ were successfully sampled during Phase 3 by coring Runs 1-3 in Hole G and coring Runs 4-6 in Hole G, respectively. Coring runs 1-3 in Hole E targeted an inferred structural boundary between sedimentary rocks of Salinian and Great Valley affinity on the west and east, respectively.

2. SAFOD Phase 3 Core Characterization

Lithology, composition, and mesoscale structural features of Phase 3 core are summarized here (Appendix A1 Table A1; Fig. 2) on the basis of descriptions made at the drill site during drilling (by J. Chester, F. Chester, D. Kirschner), at the U.S.G.S in Menlo Park, CA (by K.K. Bradbury and J. Evans), and at the IODP Gulf Coast Repository (GCR) in College Station, TX (by K.K. Bradbury and J. Evans). The descriptions (Appendix A2 Table A2) are expanded from those we prepared for the Core Photo Atlas (www.earthscope.org /safod) based on drill site descriptions. We used standard well-site and core-logging methods (Blackbourn, 1990), optical microscopy, X-ray diffraction, and X-ray fluorescence to characterize the lithology, meso- to micro-scale structure, mineral composition, and geochemistry in the near-fault environment. Detailed sample analyses were based on thirty samples taken at approximately 65 cm spacing over the entire depth range of Phase 3 spot core. Additional analyses of samples from Phase 3 core are reported in the Phase 3 Core Photo Atlas (www.earthscope.org/safod) and in several other publications [e.g., Bradbury and Evans, 2010; Chester et al., 2010; Hadizadeh, et al., 2010; Janssen et al., 2010; 2011; Morrow et al., 2010; Rybacki, et al., 2010; van Diggelen, et al., 2010; Schleicher, et al., 2010; White and Kennedy, 2010; Holdsworth et al., 2011; Lockner et al., 2011; Mittempergher, et al., 2011; Moore and Rymer, 2011).

Phase 3 core contain a compositionally heterogeneous mix of clastic sedimentary rocks fractured and sheared to different degrees (Appendix A1 Table A1; Figs. 2-4). We divide the core into several basic lithologic/structural units: arkosic sandstone (3141.4 - 3144.6 m MD and

3145.8 - 3152.6 m MD), black silty shale (3144.6 - 3145.8 m MD), black ultrafine-grained cataclasite (3193.9 – 3196.4 m MD), foliated phyllosilicate-rich fine-grained rock with heterogeneous clasts and/or interlayers that together display an overall block-in-matrix texture where blocks are composed of siltstone, sandstone, and shale (3186.7 - 3193.9 m MD, 3198.4 - 3199.5 m MD, 3294.9 – 3296.6, and 3299.1 - 3312.7 m MD), and pronounced zones of foliated fault gouge associated with the SDZ and CDZ (3196.4 – 3198 m MD and 3296.6 - 3299.1, respectively). The majority of the core is intensely fractured and sheared. The matrix of the gouge in these zones exhibits a pervasive foliation wrapping around isolated cm-scale clasts that have a strong preferred orientation (Sills et al., 2009; 2010). The westernmost multilateral hole (Hole E) encountered a mixture of arkosic sandstones and fine-grained sedimentary rocks. Three distinct rock types exist (Appendix A1 Table A1; Fig. 2-3): 1) a greenish-gray to dark-greenish gray lithic arkose (Fig. 4a); 2) a dark grayish-black silty shale/mudstone with coarser interlayers (Fig. 4b); and 3) a brownish-red feldspathic arkosic sandstone (Fig. S1a-d).

Thin white veins that are less than a mm in width and mm- to cm in length cut the green arkosic sandstone, and are oriented sub-parallel and oblique to the core axis. Several clasts within the arkosic sandstones are offset up to several millimeters by this fracture system (Fig. 4a). A second through-going fracture set, distinguished by dark reddish-brown staining, is oriented ~ 70°-130° relative to the axis of the core, and has an average spacing of ~ 30 cm (Fig. S2a). Zircon fission-track dates of cuttings from approximately the same depth suggest an average age for these rocks of approximately 64 to 70 Ma ago (Springer et al., 2009). Samples contain abundant quartz and feldspar, and minor amounts of muscovite, biotite, magnetite, chlorite, serpentine, and pyroxene (Appendix A1 Table A1). Subrounded to angular grains are supported by a fine-grained mixture of illite-smectite clays and scattered zeolites (Appendix A2 Table A2; Figs. 5a and S2a). XRF analyses indicate relatively high concentrations of Al_2O_3, likely reflecting the abundance of clays within the fine-grained matrix (Appendix A3 Table A3). In thin-section, several grains show irregular boundaries, elongated geometries, and pressure solution seams (Fig. 5a-c).

At 3144.6 m MD, a ~ 0.5 m thick interval composed of dark grayish-black silty shale/mudstone (Appendix A1 Table A1; Fig. 2) is juxtaposed with the green lithic arkose along a sharp boundary. The most notable features in the shale/mudstone interval are polished and slickenlined fracture surfaces that have a distinct vitreous luster or mineralization (Figs. 4b and

S2b). The larger, elongate, sub-angular to angular quartz and feldspar grains surrounded by fine matrix within the fractures display a weak preferred orientation, consistent with deformation and/or low-temperature neocrystallization/alteration processes (Figs. 5a-c; Appendix A1 Table A1; Yan et al., 1997; Ree et al., 2005). A distinct altered green mineral (serpentine, chlorite, and/or palygorskite?) and associated magnetite, are present in the coarser layers. Abundant opaque oxide/hydroxide grains are scattered throughout the finer-grained matrix, and are concentrated within microstylolites and irregularly shaped regions. At 3144.6 m MD, the main mineral constituents identified by XRD are quartz and plagioclase, with minor amounts of magnetite, palygorskite(?), illite, and lizardite (Appendix A2 Table A2). Lithologically, this unit is similar to rocks of the 3067 m MD fault, cored during Phase 1 (http://www.icdp-online.org/; Springer et al., 2009). Major element analyses, however, indicate that the shale/mudstone unit sampled during Phase 3 has relatively higher concentrations of Al_2O_3 and TiO_2, with a corresponding decrease in silica (Appendix A3 Table A3). Near the base or eastern boundary of this unit (~3145.8 m MD), a thin discontinuous lens of light olive-gray siltstone forms the contact with arkosic sandstone (Appendix A1 Table A1; Fig. 2). This contact is oriented at a moderate- to high-angle to the core axis. Pressure solution seams and small-scale offsets are also present near this contact (Fig. 5c).

Lower in Hole E, a reddish-brown arkosic sandstone is encountered (Figs. 2-3 and 4c). This unit is similar to the Paleocene- to Eocene arkosic sequence sampled during Phase 2 drilling and described in detail by Springer et al. (2009). Potential source rocks for the unit includes the Salinian granitic terrain and associated volcanic arc rocks (Springer et al., 2009). Dark-reddish brown lamina and coarse layers (~ 0°- 20° relative to the core axis) are offset by several through-going conjugate slip surfaces oriented at 55°-120° to the core axis with a minimum ≤ 10 cm spacing. Many of these surfaces bound mm-cm thick zones of cataclasite (Fig. S2c). Another predominate set of slip surfaces, having apparent offsets of less than 3 cm, intersect the core and are characterized by a straight fracture surface morphology. This latter set is commonly coated with a thin film of red to white clay or displays polished slickenlines that are parallel to the apparent dip (relative to the core axis) of the fracture (Fig. S2d; 30°-60° to the core axis). The primary minerals in the sandstone include quartz, feldspar, and mica (Appendix A2 Table A2). XRD analyses of the fracture coatings reveal smectite (nontronite?) clay, calcite, ± laumontite, and ± palygorskite (Appendix A2 Table A2). Pressure solution seams are comprised of fine-grained clays and/or opaque oxides/hydroxides. These features are roughly oriented sub-parallel and oblique to the dominant through-going fracture set. Microscale analyses show multiple episodes of cataclasite generation in zones < 1mm to 5 mm thick (Fig. 5d). Deformation extends beyond the discrete slip surfaces for several mm where quartz and feldspar grains greater than 0.5 mm are intensely fractured, altered, and locally show evidence for pressure solution (Fig. 5d). Development of irregular quartz grain morphologies surrounded by an interlocking network of fine-grained clay, quartz, and feldspar (Fig. 5d) suggest dissolution and neocrystallization associated with low-temperature alteration and/or fluid-rock interactions (Yan et al., 1997; Ree et al., 2005). Whole-rock geochemistry (XRF) of the arkosic sandstones west of the SDZ show elevated concentrations of SiO_2, Al_2O_3, CaO, K_2O, and Na_2O and decreased concentrations of FeO, MgO, relative to rocks sampled east of the SDZ and/or deeper in the borehole. The fracture surfaces that are coated with clays and oxides/hydroxides are one exception to the above (Appendix A3 Table A3).

Core was not collected between 3152.6 – 3186.7 m MD (Fig. 2). Over this interval, the wireline logs recorded abrupt reductions in V_p and V_s in the vicinity of 3155 m MD (Zoback et al., 2010; Fig. 1d). These velocity reductions are interpreted to represent the change in composition from arkosic sandstone to rocks rich in phyllosilicates (Jepson et al., 2010; Zoback et al., 2010). A noticeable increase in cataclasite was found in the cuttings within this interval (Bradbury et al., 2007) suggesting that this sharp boundary represents a fault.

Core collected in Hole G, from 3186.7 to 3199.5 m MD, captured a foliated cataclasite, locally displaying block-in-matrix structures, that contains clasts and blocks of siltstones and very-fine grained sandstones, and a ~3 meter interval of very fine-grained, cohesive, massive black rock (~3193.9 to 3196.4) that is interpreted to be an ultracataclasite (e.g., Janssen et al., 2010). The fine-grained matrix of the foliated cataclasite is cut by a few narrow shear zones and displays a penetrative scaly fabric that is similar to an argille scagliose fabric (Bianconi, 1840; Cowan, 1985; Pini, 1999; Vannucchi et al., 2003; Camerlenghi and Pini, 2009). The cataclasite matrix surrounds elongate, irregular-shapes lenses, clasts, and larger blocks of the sedimentary host rocks. Several clasts exhibit pinch-and-swell structures and are laced with thin, short calcite veins that do not extend into the surrounding matrix. These veins often are oriented at high angles to the matrix foliation. Black, irregular, injection-like features occur near fracture surfaces at ~3186.8, 3192.5, 3193.7, and 3989.7 m MD (Figs. 2, 4, S1, and S3; Appendix A1 Table A1).

The foliated gouge of the SDZ (Zoback et al, 2010) was intersected between 3196.4 and 3198 m MD. The boundary of the gouge with the foliated cataclasite to the west is sharp, compositionally distinct, and oriented at a high angle to the core axis (Figs. 2, 3, and 7). The matrix of the gouge is an incohesive, dark grayish-black to greenish-black phyllosilicate-rich, ultra fine-grained zone that displays a scaly fabric with pronounced anastomosing polished slip surfaces. Clasts of the surrounding host rocks, including serpentine, are dispersed throughout the gouge and account for up to 10% of the total gouge volume (Sills, 2010) (Appendix A1 Table A1; Fig. S3d). In contrast to the pinch-and-swell textures and fractured clasts of the foliated caltaclasites to the east, the clasts within the foliated gouge are elongate, have smooth boundaries (Sills, 2010), and exhibit a greater degree of alteration (Fig. 7). Lens-shaped fragments or phacoids of the gouge matrix (Figs. S3d and 7), split apart easily and reveal polished and sometimes striated surfaces. A ~ 30 cm thick block of massive, serpentinite occurs within the foliated gouge interval. The boundaries of this block also are sharp and oriented at a high angle to the core axis. The block is cut by numerous white (calcite and chrysotile) veins that are up to several mm-thick and are oriented sub-parallel to the core axis (Fig. 7). The eastern boundary of the serpentinite block is defined by a 4-cm-thick zone of altered and sheared blue-green serpentinite that displays an earthy luster and contains fragmented veins oriented roughly perpendicular to the core axis. (Appendix A1 Table A1; Fig. 7a). Clasts of serpentinite within the core catcher are sheared and appear altered, and generally are elongated parallel to the foliation (Figs. S3d and 7).

The small section of core captured to the east of the SDZ in Hole G displays considerably less deformed sedimentary rock. Within the blocks or interlayers, bedding is intact and defines alternating layers of finely laminated, light gray to gray-green, fine-grained silty sandstone and silty shale/mudstone (Fig. S1d). Calcite veins dissect the silty sandstone but terminate abruptly against the shaley layers (Fig. S1d). Contacts between laminae in some cases appear to be dark seams with stylolitic geometries and may suggest solution processes. Clay smears are developed along the mesoscopic slip surfaces that are oriented at high-angles to the core axis. Quartz and plagioclase (albite) are the predominate minerals comprising the siltstone layers. Veins of calcite and chlorite ± smectite ± illite phases are noted in the sheared shaley layers (Appendix A2 Table A2a-b). Serpentine (lizardite and chrysotile) was also noted in some analyses of the clasts within the foliated gouge materials at 3197.9 m MD (Appendix A2 Table A2).

No core was collected between 3199.5 m MD and 3294.9 m MD. Hole G (Runs 4, 5, and 6) captures rock from 3294.9 - 3312.7 m MD. Over this interval the lithology and deformation vary significantly. Core Run 4 intersected a distinctive, interlayered Mg-rich siltstone and sandstone unit that is cut by numerous mesoscale faults and finer, more distributed shear surfaces (Appendix A1 Table A1-A2).

The foliated gouge layer of the CDZ was intersected between 3296.6 and 3299.1 m MD, correlating to the region of active casing deformation at 3302 m MD in the main borehole (Zoback et al., 2010; Appendix A1 Table A1; Figs. 1-3, 8, S4). The matrix of the CDZ is remarkably similar to that of the SDZ, consisting of phyllosilicate-rich gouge with a penetrative foliation that is oriented approximately perpendicular to the core axis (Fig. S4). Like the SDZ, the gouge contains matrix-supported, elongate clasts that parallel the foliation (Figs. S5 and 8a-b; Sills et al., 2009). The boundaries of several clasts are sheared, and many display numerous calcite veins, some up to 1 to 2 mm wide (Fig. 8b). Whole-rock XRD powder samples near ~ 3297 m MD indicate the presence of saponite, serpentine (lizardite ± chrysotile), quartz, and feldspar (Appendix A2 Table A2). Geochemical data from this interval show significantly elevated concentrations of MgO and Ni-oxides, suggesting potential fluid-assisted alteration of serpentinite (O' Hanley, 1996; Appendix A3 Table A3; Fig. S5). These data are consistent with those reported by others (e.g., Schleichler et al., 2010; Holdsworth et al., 2010; Moore and Rymer, 2011).

East of the CDZ, there is a mixture of alternating fine-grained sandstone, siltstone, and shale that is fractured and sheared to varying degrees. The dimensions of deformed blocks range up to 190 mm (Figs. 4 and S1). The long axes of the blocks exhibit a preferred orientation that is inclined ~ 40° to 90° to the core axis. In general, the block size increases towards the base of Hole G with a corresponding decrease in block asymmetry. Exceptions to the overall trend occur within the comminuted, fine-grained shear zones. Slip surfaces bounding the blocks, and layers of cataclasite, breccia, and noncohesive rubble are inclined ~ 40 to 50° to the core axis. Polished, striated surfaces on disaggregated fragments are nearly ubiquitous throughout Hole G. Meso-scale sulfide lenses, concretions, and nodules are present throughout the core and increase in occurrence towards the base of Hole G. Gouge and other highly sheared fault rocks within Hole G (Black fault rock, SDZ, and CDZ in Appendix A1 Table A1) account for over 13 % by volume of the total core sampled. Cuttings below ~3313 m MD contain a greater number of cataclasite fragments and show a greater degree of alteration (Bradbury et al., 2007), supporting the suggestion that fault-related damage extends further east and to deeper depths (Zoback et al., 2010).

Numerous veins, approximately 1-mm-thick, cut the Phase 3 core. These primarily are concentrated within the sandstones, but also lace the serpentinite blocks and the black ultra-fine grained rocks surrounding the SDZ and CDZ (Figs. 6 and 7). Cross-cutting relationships suggest that there were at least two episodes of vein formation (Figs. 6-8).

4. Discussion

We characterize the SAFOD Phase 3 core samples from the San Andreas Fault zone at approximately ~ 3 km depth as compositionally heterogeneous and structurally complex at the meter scale, i.e., at a scale that is important to earthquake rupture nucleation and propagation (Sibson, 2003). The ~ 41 m of core is comprised of a mixture of fractured arkosic sandstones, penetratively sheared siltstones and shales, cataclasite to ultracataclasite, and foliated serpentinite-bearing clay fault gouge, alternating with blocks of less-deformed fine-grained sandstone and siltstone. Over 60% by volume of the core is comprised of sheared phyllosilicate-rich layers, gouge and ultracataclasite, and lenses of other fault rocks (Fig. 2).

West of the SDZ, at a MD of approximately 3150 m (Zoback et al., 2010), the arkosic rocks exhibit localized brittle structures documenting evidence for repeated episodes of deformation. These structures display variations in the composition and texture of fracture-fill, differences in shear fracture morphology, and distinct cross-cutting relationships (Tables A1-A3). The structural relations are consistent with episodic fluid-rock interactions and brittle fault-related damage generation associated with slip on the San Andreas Fault. Generation of fault-related damage farther west of 3150 m MD also is indicated by structures observed in image logs, features of cuttings, and core-samples collected during Phases 1 and 2 (Bradbury et al., 2007; Springer et al., 2009). The approximately 200 m-thick damage zone identified between 3192 and 3413 m MD on the basis of seismic velocity, resistivity and other log data (Zoback et al., 2010) is likely a minimum estimate of the total extent of fault-related damage. On the basis of core studies, a better estimate would be at least 350 m, starting at 3050 m MD (Chester et al., 2007, 2010; Heron et al., 2011; Jeppson et al., 2010). The intensity of damage does not appear uniform within this interval, and likely reflects the presence of multiple principal slip surfaces and fault rock lenses with overlapping damage zones. In addition, it is unlikely that all surfaces and damage zones are active at any one time (Malin et al., 2006; Chester et al., 2010).

Along the western boundary of the SDZ, the sheared black and black-stained rocks (Figs. 4 and S1) that contain injection structures (Figs. 6e-f and S3b-c) and foliated cataclasite (Fig. 6e-f) are unique. Geochemical analyses indicate that these rocks are rich in carbonaceous material (Fig. 3). The localized black staining may indicate hydrocarbons are migrating or have recently migrated along fractures in the SDZ. Two distinct mud gas-rich zones were identified in the SAFOD borehole at 2700 - 2900 m MD and at depths greater than 3550 m MD. Smaller interstratified lenses rich in CO_2 and hydrocarbons were found between 3150-3200 m MD, and nearly pure hydrocarbons exist between 3310-3340 m MD (Fig. 2; Wiersberg and Erzinger; 2008). Additionally, small tar seeps are present along the surface trace of the SAF up-dip of the SAFOD borehole. Oxygen and carbon isotopes within carbonate veins located throughout the Phase 3 core, including the SDZ and CDZ, also are consistent with carbonates having precipitated from a fluid charged with hydrocarbons (Kirschner et al., 2008). Given the regional geology, the source of hydrocarbons likely is the Great Valley Formation (Ingersoll et al., 1977).

Janssen et al. (2010) cited evidence for comminuted materials similar to crush-origin pseudotachylytes within the black rocks at ~3194 m MD, based on SEM and TEM observations, and Holdsworth et al. (2011) suggests these textures are related to local fluidization or injection during transient overpressure of pore fluids during slip events. Similar features are found in active and ancient fault zones elsewhere and have been attributed to a mixture of comminution, fluidization, and thermal pressurization processes (Ujiie et al., 2007; Rowe et al., 2005; Wibberley and Shimamoto, 2005; Brodsky et al., 2009; Meneghini et al., 2010). While we observe injection- and fluidization-type features at the microscale (Fig. 6b), diagnostic evidence for pseudotachylyte in our samples is absent at the optical scale. Accordingly, the black rocks (Figs. 6 and S3) may reflect: 1) ancient ultracataclasite, and thus, as suggested by Holdsworth et al. (2011) could be regions that slipped seismically in the past; 2) a concentration of damage associated with repeated microearthquakes; and 3) hydrocarbon migration and gas-charged fluids entering fractures during deformation, associated with transient fluid pressure changes (Mittempergher et al., 2011).

The block-in-matrix structures and scaly clay fabrics that characterize the regions surrounding the SDZ and CDZ (Figs. 3-4) are similar to block-in-matrix structures of sedimentary rock in tectonic mélange (Hsü, 1968; Raymond, 1984; Medley and Goodman, 1994; Festa et al., 2010). Although similar scaly clay fabrics are observed in numerous exhumed exposures of Franciscan mélange and in sheared serpentinite outcrops within the San Andreas Fault system (Bradbury and Evans, 2009; Moore and Rymer, 2009, 2010), these rocks do not display diagnostic mineralogical assemblages or conclusive evidence of originating from the Franciscan tectonic mélange. The rocks may result from 1) repeated episodes of deformation, fragmentation, and mixing related to strike-slip faulting (Fagereng and Sibson, 2010; Festa et al., 2010) producing foliated cataclasite; 2) pre-SAF deformation of the protolith, e.g. slivers of altered Franciscan mélange entrained within the fault zone; or 3) a combination of SAF-related shearing superposed on the initial block-and-matrix mélange fabric. Given the penetrative nature of the thin, anastomosing surfaces within the matrix encompassing the blocks, the block-in-matrix structure may reflect continuous deformation processes related to aseismic creep and stable frictional sliding (Faulkner et al., 2003; Colletini et al., 2009).

The penetrative and highly sheared scaly fabric of the serpentinite-bearing, clay-rich fault gouge that correlates with the actively creeping SDZ and CDZ, reflects the presence of meso- to micro-scale anastomosing slip surfaces that are coated with clays and opaque oxide-hydroxides. These surfaces locally weave around lens-shaped porphyroclasts of compacted matrix material (Sills et al. 2010), reworked cataclasite, and other lithologies, and display striated and polished slip surfaces (Figs. 6-8). Schleicher et al. (2010) identify illite-smectite and chlorite-smectite as the main phases comprising the clay coatings along such surfaces within the matrix materials near ~3066 m and ~3300 m MD, and suggest these coatings may influence slip and aseismic creep through dissolution-precipitation processes. Experimental work on clay-rich samples from SAFOD and other exhumed fault rocks also demonstrates the potential for clay to influence the frictional properties of clay-lined fractures (e.g., Tembe et al., 2006; Morrow et al., 2007; Solum and van der Pluijm, 2009).

The composition and distribution of serpentinite and related alteration products may play a key role in the evolving mechanical behavior of the SAF system in the region (Reinen et al., 1991; Moore, 1996; 1997; 2007, 2009, 2010). Saponite, the Mg-rich smectite phase that is an alteration product of serpentinite in the presence of fluids (e.g., Moore and Rymer, 2010), is very abundant within the SDZ and CDZ gouge (Appendix A2 Table A2) and frequently comprises alteration rims on serpentinite clasts. Saponite is very weak in shear and displays a coefficient of sliding friction that approaches $\mu = 0.05$ (Morrow et al., 2010; Lockner et al., 2011). The XRD analyses of samples indicate the foliated gouge contains significant quantities of lizardite and chrysotile. Experimental work has demonstrated that small amounts (<15% bulk wt. %) of serpentine may significantly reduce the overall frictional strength of fine-grained materials (Escartin et al., 2001), though even high concentrations of serpentine do not lead to friction coefficients as low as seen in smectites (e.g., Morrow et al., 1984; 2000; Moore et al., 1996; 1997; Reinen, 2000; Evans, 2004; Andreani et al., 2005). Many previous field studies have noted the presence of serpentinite and weak clays along the central segment of the SAF, and numerous laboratory experiments have explored the mechanical role of these phases in promoting fault creep (e.g., Allen, 1968; Irwin and Barnes, 1975; Reinen et al., 1991; Ikari et al., 2009). Data from these studies suggest that these phases can explain fault zone weakening, nondilatant brittle deformation, and the aseismic creep, and they may influence the fluid-flow properties of the fault zone locally (e.g., Escartin, et al., 1997; Carpenter et al., 2009; 2011; Solum and van der Pluijm, 2009; Schleicher et al., 2009; Morrow et al., 2000; 2007; Lockner et al., 2011). These suggestions are supported by the correlation of active creep in the chemically and mineralogically distinct foliated gouge layers rich in serpentinite and saponite (e.g., Moore and Rymer, 2010).

Geochemical data from the core shows that the major element composition of the SDZ and CDZ is dramatically different than the surrounding rocks (Bradbury and Evans, 2010). This is consistent with data presented by Holdsworth et al. (2010) on several other samples. Core samples from rock in Hole E, and farther west, have higher levels of Al_2O_3 with moderate to higher levels of SiO_2 as compared to core samples taken to the east (Fig. S5a). In the SDZ, MgO concentrations are elevated significantly compared to surrounding host rocks and show a corresponding decrease in SiO_2 (Fig. S5c). SiO_2 concentrations are variable in sampled rocks between the SDZ and CDZ and are associated with relative increases in Al_2O_3 or CaO (Fig. S5d). Within the CDZ, MgO concentrations are once again elevated with SiO_2 decreasing (Fig. S5e). In both the SDZ and CDZ, elemental Ni and Cr concentrations are elevated (Appendix A3 Table A3), approaching ore-grade values (Candela and Piccoli, 2005), and may suggest either significant fluid-assisted alteration of serpentinite to clay (O'Hanley, 1996) or represent mineralogical signatures potentially inherited from the protolith material. East of the CDZ to ~

3313 m MD, SiO_2 levels are again highly variable with associated increases in Al_2O_3 levels (Fig. S5f).

Isotopic data identifies at least two populations of carbonate veins showing variable composition in the host rocks, whereas elements such as strontium and calcium are more uniformly distributed inside the foliated gouge of the SDZ and CDZ (Kirschner et al., 2008). Thus, it appears the incorporation of serpentinite into the two layers of foliated gouge, mechanical mixing and grain size reduction, and the alteration to clay, combine to produce profoundly weak layers of gouge and promote long-lived concentrated shear and aseismic creep along the SDZ and CDZ intersected by the borehole at SAFOD.

5. Conclusions

In situ sampling and laboratory analysis of SAFOD Phase 3 core samples provides an opportunity to characterize the composition, internal structure, and weakening processes of an active fault zone undergoing shear and fluid-rock reactions at approximately 3 km depth. Combining core-scale descriptions and analysis of 30 samples collected across the SAF zone, we find the fault zone consists of broad zone of variable damage (> 300 m wide) that surrounds multiple narrower zones of highly sheared and altered rock containing complex internal structures. West of the SDZ, arkosic sequences and shales exhibit brittle deformation features and evidence of cementation. Adjacent to the southwest boundary of the SDZ, black fault rocks contain evidence of multiple episodes of slip and cataclasite and ultracataclsite generation with increases in magnetite,iron-sulfides, and organic carbon. Serpentinite- and smectite-bearing foliated gouge layers correlating with the SDZ and CDZ display highly sheared, scaly fabrics with a significant enrichment in Mg-rich clays, and Ni- and Cr-oxides relative to the surrounding rocks. The northeastern boundary of the CDZ is characterized by increases in magnetite and iron-sulfide. These data point to the influence of both mechanical and chemical processes of weakening and localization of shear to at least two discrete and active zones of creep in the SAFOD borehole.

ACKNOWLEDGEMENTS

This work was supported by NSF-EarthScope grants EAR-044527 and 0643027 to Evans, EAR-0454525 and EAR-0643339 to J. Chester and F. Chester, and EAR-0346190 and -454531 to Kirschner. Bradbury received supplementary support for sample analyses and travel to the IODP Gulf Coast Repository (GCR) from DOSECC, SEG Foundation, AAPG, SPWLA Foundation, and the GDL Foundation. XRF analyses were performed by WSU laboratory. We thank Bradley Weymer and Phil Rumford at the GCR Laboratory for cutting and processing the SAFOD core, their patience in helping us to obtain our core samples, and for their efforts towards caring and preserving this core. A special thanks is due to USU Undergraduate student, Dave Richie, for help grinding several samples for XRD analyses. Finally, we thank the principal investigators of the SAFOD project, William Ellsworth, Steven Hickman, and Mark Zoback for their hard work and dedication to the SAFOD project, and to Diane Moore and an anonymous reviewer for thoughtful reviews of this manuscript.

References

Allen, C.R., 1968. The tectonic environments of seismically active and inactive areas along the San Andreas Fault system, in: Dickinson, W.R. Grantz, A. (Eds.), Proc. of Conf. on Geologic Problems of the San Andreas Fault, Stanford Univ. Pub. Geol. Sci. XI, Stanford, CA, pp. 70-82.

Almeida, R., Chester, J.S., Chester, F.M., Kirschner, D.L., Waller, T.D., Moore, D.E., 2005. Mesoscale structure and lithology of the SAFOD Phase 1 and II core samples. EOS Trans., AGU, 86(52) T21A-0454.

Andreani, M., Boullier, A.-M., and Gratier, J.-, 2005. Development of schistosity by dissolution—crystallization in a Californian serpentinite gouge. J. Struc. Geol. 27, 2256-2267, doi: 10.1016/j.jsg.2005.08.004.

Bailey, E.H., Irwin, W., and Jones, D.L., 1964. Franciscan and related rocks, and their significance in the geology of western California. California Division of Mines and Geology Bulletin 183, pp. 177.

Bianconi, G., 1840. Storia naturale dei terreni ardenti, dei vulcani fangosi, delle sorgenti infiammabili, dei pozzi idropirici e di altri fenomeni geologici operati dal gas idrogene e della origine di esso gas, Marsigli, Bologna (1840) pp. 164.

Blackbourn, G.A. 1990, Cores and Core Logging, Whittles Publishing, pp. 113.

Bombolakis, E.G., Hepburn, J.C., and Roy, D.C., 1978. Fault creep and stress drops in saturated silt-clay gouge: J. Geophys. Res. 83, B2, 818-829.

Boness, N.L., and Zoback, M.D., 2006, A multiscale study of the mechanisms controlling shear velocity anisotropy in the San Andreas Fault Observatory at Depth: Geophysics, 71, F131–F146, doi: 10.1190/1.2231107.

Bradbury, K.K., Barton, D.C., Solum, J.G., Draper, S.D., and Evans, J., 2007, Mineralogic and textural analyses of drill cuttings from the San Andreas Fault Observatory at Depth (SAFOD) boreholes: Initial interpretations of fault zone composition and constraints on geologic models: Geosphere, 3, 299-318, doi: 10.1130/GES00076.1.

Bradbury, K.K. and Evans, J.P., 2009, Franciscan Formation within the SAFOD Borehole, near Parkfield, CA, Geol. Soc. of America Abst.with Prog., 41, 7., 404.

Bradbury, K.K., and Evans, J.P., 2010, Rock properties and internal structure of the San Andreas Fault near ~ 3 km depth in the SAFOD borehole based on meso- to micro-scale analyses of Phase III whole rock core, Abstract T41A-2099 presented at 2010 Fall Meet., AGU, San Francisco, CA, 13-17 Dec.

Brodsky, E.E., Rowe, C.D., Meneghini, E., and Moore, J.C., 2009, A geological fingerprint of low-viscosity fault fluids mobilized during an earthquake: J. Geophys. Res., 114, B01303, doi: 10.1029/2008JB005633.

Caine, J.S., Evans, J., and Forster, C.B., 1996, Fault zone architecture and permeability structure: Geology, 24, 11, 1025-1028, doi:10.1130/0091-7613.

Candela, P.A. and Piccoli, P.M., 2005, Magmatic Processes in the Development of Porphyry-type Ore Systems. Society of Economic Geologists 100 th Anniversary Volume, *in* Hedenquist, J.W., Thompson, J.F.H., Goldfarb, R.J., and Richards, J.P. (Eds.), p. 25-38.

Camerlenghi, A., and Pini, G.A., 2009, Mud volcanoes, olistostromes and argille scagliose in the Mediterranean region: Sedimentology, 56, 319-365, doi: 10.1111/j.1365-3091.2008.01016.x.

Carpenter, B.M., Marone, C., and Saffer, D.M., 2009, Frictional behavior of materials in the 3D SAFOD volume: Geophys. Res. Lett., 36, L05302, doi: 10.1029/2008GL039990, 2009.

Carpenter, B.M., Marone, C., and Saffer, D.M., 2011, Weakness of the San Andreas Fault revealed by samples from the active fault zone: Nature Geoscience, AOP, doi:10.1038/NGE01089.

Chester, F.M., and Logan, J.M., 1986, Implications for mechanical properties of brittle faults from observation of the Punchbowl fault zone, California: Pageoph, 124, 79–106, doi: 10.1007/BF00875720.

Chester, F.M., Evans, J., and Biegel, R.L., 1993, Internal structure and weakening mechanisms of the San Andreas Fault: J. Geophys. Res., 98, 771–786.

Chester, J.S., Chester, F.M., Sills, D.W., Heron, B., Almeida, R.V., and Guillemette, R.N., 2010, Structure of the San Andreas Fault at SAFOD: Abstract T52B-03 presented at 2010 Fall Meet., AGU, San Francisco, CA, 13-17 Dec.

Chester, J.S., Chester, F.M., Kirschner, D.L., Almeida, R., Evans, J.P., Guillemette, R.N., Hickman, S., Zoback, M, Ellsworth. B., 2007, Deformation of Sedimentary Rock Across the San Andreas Fault Zone: Mesoscale and Microscale Structures Displayed in Core From SAFOD, Eos Trans. AGU, 88(52), T42C-05.

Colletini, C., Niemeijer, A., Viti, C., and Marone, C., 2009, Fault zone fabric and fault weakness: Nature, 462, 907-910, doi: 10.1038/nature08585.

Cowan, D.S., 1985, Structural styles in Mesozoic and Cenozoic mélanges in the western Cordillera of North America: Geol. Soc. Amer. Bull., 96, 451-462, doi: 10.1130/0016-7606(1985)96<451:SSIMAC> 2.0.CO;2.

Dibblee, T.W., 1971, Geologic maps of seventeen 15-minute quadrangles along the San Andreas Fault in the vicinity of King City, Coalinga, Panoche Valley, and Paso Robles, California: U.S. Geological Survey Open-File Report OF-71–87, scale 1:62,500.

Dibblee, W.T., 1973, Stratigraphy of the southern Coast Ranges near the San Andreas Fault from Cholame to Maricopa, California, U. S. Geological Survey Prof. Paper 764.

Dickinson, W.R., 1966, Table Mountain serpentinite extrusion in California Coast Ranges: Geol. Soc. Amer. Bull., 77, 451–472, doi: 10.1130/0016-7606(1966)77[451:TMSEIC]2.0.CO;2.

Ellsworth, W., Hickman, S., Zoback, M.D., Davis, E., Gee, L., Huggins, R., Krug, R., Lippus, C., Malin, P., Neuhauser, D., Paulsson, B., Shaley, E., Vajapevam, B., Weiland, C., and Zumberge, M., 2005, Observing the San Andreas Fault at depth, Eos Trans. AGU, 86, (52), Fall Meet., Suppl., Abstract T24B-04.

Escartin, J., Hirth, G., and Evans, G., 1997, Nondilatant brittle deformation of serpentinites: implications of Mohr-Coulomb theory and the strength of faults: J. Geophys. Res., 102, B2, 2897-2913, doi: 10.1029/96JB02792.

Escartin, J., Hirth, G., and Evans, G., 2001, Strength of slightly serpentinized periodotites: implications for the tectonics of oceanic lithosphere: Geology, 29, 11, 1023-1026, doi: 10.1130/0091-7613.

Evans, B.W., 2004, The serpentinite multisystem revisited in Ernst, W.G., (Ed.), Serpentine and serpentinites: mineralogy, petrology, geochemistry, ecology, geophysics, and tectonics, A tribute to Robert G. Coleman, International book series 8, 5-32.

Evans, J. P., 1990, Textures, deformation mechanisms, and the role of fluids in the cataclastic deformation of granitic rocks *in*: Knipe, R. J. and Rutter, E. H. (Eds.), Deformation Mechanisms, Rheology and Tectonics, Leeds, England, The Geological Society of London, p. 29-39.

Evans, J.P. and F.M. Chester, 1995, Fluid-rock interaction in faults of the San Andreas system: Inferences from San Gabriel fault rock geochemistry and microstructures, Journal of Geophysical Research, v. 100, no. B7, p. 13007-13020.

Evans, J., Forster, C.B., and Goddard, J., 1997, Permeabilities of fault-related rocks and implications for fault-zone hydraulic structure: J. of Structural Geology, 19, 1393–1404, doi: 10.1016/S0191-8141(97)00057-6.

Fagereng A., and Sibson, R.H., 2010, Melange rheology and seismic style: Geology, 38, 8, 751-754, doi: 10.1130/G30868.1.

Faulkner, D.R., Lewis, A.C., and Rutter, E.H., 2003, On the internal structure and mechanics of large strike-slip fault zones; field observations of the Carboneras Fault in southeastern Spain: Tectonophysics, 367, 235–251, doi: 10.1016/S0040-1951(03)00134-3.

Festa, A., Pini, G., Dilek, Y., and Codegone, G., Melanges and mélange-forming processes: a historical overview and new concepts: Intl. Geol. Review, 52, 10-12, 1040-1105, doi:10.1080/00206810903557704.

Hadizadeh, J., Gratier, J.L., Mittempergher, S., Renard, F., and Richard, J., Implications of Microstructural studies of the SAFOD gouge for the strength and deformation mechanisms in the creeping segment of the San Andreas Fault, Abstract T41A-2100 presented at 2010 Fall Meet., AGU, San Francisco, CA, 13-17 Dec.

Harris, R. A. and Arrowsmith, J. R., 2006, Introduction to the Special Issue on the 2004 Parkfield Earthquake and the Parkfield Earthquake Prediction Experiment: Bull. Seism. Soc. Amer., 96, 4B, S1-S10, doi: 10.1785/0120050831.

Heron, B., Chester, J.S., Chester, F.M., Guillemette, R., 2011, Densification and Alteration of Siliciclastics Adjacent to the San Andreas Fault at SAFOD: Implications for Seismic Velocity Structure and Fluid Flow, AAPG Abstracts with Programs #90124.

Hickman, S., Zoback, M. D., and Ellsworth, W., 2004, Introduction to special section: Preparing for the San Andreas Fault Observatory at Depth, Geophys. Res. Lett., 31, L12S01, doi:10.1029/2004GL020688.

Hickman, S., Zoback, M., Ellsworth, W., Boness, N., Malin, , Roecker, S., and Thurber, C., 2007, Structure and properties of the San Andreas Fault in central California: recent results from the SAFOD experiment: Scientific Drilling, Special Issue 1., 29-32, doi: 10.2204/iodsd.s01.2007.

Holdsworth, R.E., van Diggelen, E.W.E., de Bresser, J.H.P., Walker, R.J., and Bowen, L., 2011, Fault rocks from the SAFOD core samples: Implications for weakening at shallow depths along the San Andreas Fault, California, Jour. of Struct. Geol, 33, 2, 132-144, doi:10.1016/j.jsg.2010.11.010.

Hole, J.A., Ryberg, T., Fuis, G.S., Bleibinhaus, F., and Sharma, A.K., 2006, Structure of the San Andreas Fault zone at SAFOD from a seismic refraction survey: Geophys. Res. Lett., 33, L07312, 1-4, doi: 10.1029/2005GL025194.

Hsü, K.J., 1968, Principles of Mélanges and their Bearing on the Franciscan-Knoxville Paradox: Geol. Soc. Amer. Bull., 79, 1063-1074, doi: 10.1130/0016-7606(1968)79.

Ikari, M.J., Saffer, D.M., and Marone, C., 2009, Frictional and Hydrologic properties of clay-rich fault gouge: J. Geophys. Res., 114, B05409, doi: 10.1029/2008JB006089.

Ingersoll, R., Rich, E.I., and Dickinson, W.R., 1977, Great Valley Sequence, Sacramento Valley, California: Geolocial Society of America Cordilleran Secion Fieldtrip Guidbook, 72.

Irwin W., and Barnes, I., 1975, Effect of geologic structure and metamorphic fluids on seismic behavior of the San Andreas Fault system in central and northern California: Geology, 3, 12, 713-716, doi: 10.1130/0091-7613.

Isaacs, A.J., Evans, J., Song, S-R., Kolesar, T., 2007, Structural, mineralogical, and geochemical characterization of the Chelungpu Thrust Fault, Taiwan, Terr. Atmos. Ocean. Sci., Vol. 18, 2, 183-221.

Janssen, C., R. Wirth, R. Rybacki, E. Naumann, H. Kemnitz, H.-R. Wenk, and G. Dresen, 2010, Amorphous material in SAFOD core samples (San Andreas Fault): Evidence for crush origin pseudotachelytes? Geophys. Res. Lett., 37, L01303, doi: 10.1029/2009GL040993.

Janssen, C., R. Wirth, R. Reinicke, A., Rybacki, E., Naumann, H., H.-R. Wenk, and G. Dresen, 2011, Nanoscale porosity in SAFOD core samples (San Andreas Fault), Earth and Planetary Science Letters, V. 301, 1-2, p. 179-189.

Jeppson, T.N., Bradbury, K.K., and Evans, J.P, 2010, Geophysical properties of the San Andreas Fault zone a the San Andreas Fault Observatory at Depth (SAFOD) and their relationship to rock properties: J. Geophys. Res., doi:10.1029/2010JB007563.

Kirschner, D.L., Chester, J., Chester, F., Evans, J., and Hickman, S., 2008, Stable Isotope Data of Veins From the 2007 SAFOD Core: Eos Trans. AGU 89 (53) Fall Meet. Suppl. Abstract T51A-1850.

Knipe, R. J., 1993, The influence of fault zone processes and diagenesis on fluid flow *in*: Horbury, A. D. and Robinson, A. G. (Eds.), Diagenesis and Basin Development, AAPGStudies in Geology #36, p. 135-148.

Li, Y.G., Vidale, J.E., and Cochran, E.S., 2004, Low-velocity damaged structure of the San Andreas Fault at Parkfield from fault zone trapped waves: Geophys. Res. Lett., 31, L12S06, doi: 10.1029/2003GL019044.

Li, Y.G., and Malin, E., 2008, San Andreas Fault damage at SAFOD viewed with fault-guided waves: Geophys. Res. Lett., 35, L08304, doi: 10.1029/2007GL032924.

Lockner, D.A., Morrow, C., Moore, D., and Hickman, S., 2011, Low strength of deep San Andreas fault gouge from SAFOD core, Nature, 472, p. 82-85, doi:10.1038/nature09927.

Malin, O., Shalev, E., Balven, H., Lewis-Kenedi, C., 2006, Structure of the San Andreas Fault at SAFOD from P-wave tomography and fault-guided wave mapping, Geophys. Res. Lett., 33, L13314, doi:10.1029/2006GL025973.

McPhee, D.K., Jachens, R. C., and Wentworth, C. M., 2004, Crustal structure across the San Andreas Fault at the SAFOD site from potential field and geologic studies, Geophys. Res. Lett., 31, L12S03, doi: 10.1029/2003GL019363.

Medley, E.W., and Goodman, R.E., 1994, Estimating the block volumetric proportions of mélanges abd similar block-in-matrix rocks (bimrocks) in Nelson, , and Laubauch, S.E., (Eds.), Rock Mechanics Models and Measurement Challenges from Industry, Proceedings, 1st North American Rock Mechanics Symposium, Austin, TX, May 1994, 851-858.

Meneghini , F., Di Toro, G., Rowe, C.D., Moore, J.C., Tsutsumi, A., and Yamaguchi, A., 2010, Record of mega-earthquaks in subduction thrusts: the black fault rocks of Pasagshak Point (Kodiak Island, Alaska): Geol. Soc. Amer. Bull., 122, 7/8, 1280-1297, doi: 10.1130/B30049.1.

Mittempergher, S., Toro, G.D., Gratier, J.P., Hadizadeh, J., Smith, S., 2011, Evidence of transient increases of fluid pressure in SAFOD Phase III Cores: Geophys. Res. Lett., 38, L03301, doi:10.1029/2010GL046129.

Moore, D.E., Lockner, D.A., Summers, R., Shengli, M., and Byerlee, J.D., 1996, Strength of chrysotile-serpentinite gouge under hydrothermal conditions: can it explain a weak San Andreas Fault: Geology, 24, 1041-1044, doi: 10.1130/0091-7613.

Moore, D.E., Lockner, D.A., Shengli, M., Summers, R., and Byerlee, J., 1997, Strengths of serpentinite gouges at elevated temperatures: J. Geophys. Res., 102, 14787-14801, doi:10.1029/97JB00995.

Moore, D.E., and Rymer, M.J., 2007, Talc-bearing serpentinite and the creeping section of the San Andreas Fault: Nature, 448, 795-797, doi: 10.1038/nature06065.

Moore, D.E., and Rymer, M.J., 2009, Clay rich fault gouge identified in serpentinite from the San Andreas Fault zone at Nelson Creek, Monterey County, California, AGU Fall Meet. 2009, Abstract T53C-1599.

Moore, D.E., and Rymer, M.J., 2010, Metasomatic origin of fault gouge comprising the two actively creeping strands at SAFOD, AGU 2010 Fall Meet., San Francisco, CA, 13-17 Dec., Abstract T41A-2105.

Morrow, C.A., Shi, L.Q., and Byerlee, J.D., 1984, Permeability of fault gouge under confining pressure and shear stress: J. Geophys. Res., 89, B5, 3193-3200, doi:10.1029/JB089iB05p03193.

Morrow, C.A., Moore, D.E., and Lockner, D.A., 2000, The effect of mineral bond strength and adsorbed water on fault gouge frictional strength: Geophys. Res. Lett., 27, 6, 815-818.

Morrow, C., J. Solum, S. Tembe, D. Lockner and T.F. Wong, 2007, Using drill cutting separates to estimate the strength of a narrow shear zones at SAFOD: Geophys. Res. Lett., 34, 11, L11301.

Morrow, C..A., Lockner, D.A., Moore, D.E., and Hickman, S., 2010, SAFOD core reveals low strength of deep San Andreas Fault gouge and provide explanation for low heat flow in creeping section of fault, AGU 2010 Fall Meet., San Francisco, CA, 13-17 Dec., Abstract T52B-05.

O'Hanley, D.S., 1996, Serpentines: Records of Tectonic and Petrological History: Oxford University Press, 269.

Ohtani, T., Fujimoto, K., Ito, H., Tanaka, H., Tomida, N., and Higuchi, T., 2000, Fault rocks and past to recent fluid characteristics from the borehole survey of the Nojima fault ruptured in the 1995 Kobe earthquake, southwest Japan: J. Geophys. Res., 105, 16161–16171, doi: 10.1029/2000JB900086.

Page, B.M., Thompson, G.A., and Coleman, R.G., 1998, Late Cenozoic tectonics of the central and southern Coast Ranges of California: Geol. Soc. Amer. Bull., 110, 846–876, doi: 10.1130/0016-7606(1998)110<0846:OLCTOT>2.3.CO;2.

Pares, J.M., Schleicher, A.M., van der Pluijm, B.A., and Hickman, S.H., 2008, Paleomagnetic reorientation of San Andreas Fault Observatory at Depth (SAFOD) core: Geophys. Res. Lett., 35, L02306, doi: 10.1029/2007GL030921.

Pini, G.A., 1999, Tectonosomes and olistostromes in the Argille Scagliose of the Northern Apennines, Italy: Geol. Soc. Amer. Spec. Paper 335, 71.

Raymond, L.A., editor, 1984, Melanges: Their nature, origin, and significance: Geol. Soc. Amer. Spec. Paper 198, 170.

Reches, Z., and Ito, H., 2007, Scientific Drilling of Active Faults: Past and Future, *in:* Harms, U., Koeberl, C., and Zoback, M.D., (eds.), Continental Scientific Drilling, 235-258, doi:10.1007/978-3-540-68778-8_6.

Ree, J-H., Kim, H.S., Han, R., and Jung, H., Grain-size reduction of feldspars by fraturing and neocrystallization in a low-grade mylonite and its rheological effect, Tectonophysics, 407, p. 227-237, doi: 1010.1016/j/tecto.2005.07.010.

Reinen, L.A., Weeks, J.D., and Tullis, T.E., 1991, The frictional behavior of serpentinite: implications for asesimic creep on shallow crustal faults: Geophys. Res. Lett., 18, 10, 1921-1924.

Reinen, L.A., 2000, Seismic and aseismic slip indicators in serpentinite gouge: Geology, 28, 135-138, doi: 10.1130/0091-7613(2000)28<135:SAASII>2.0.CO;2.

Rowe, C.D., Moore, J.C., Meneghini, F., and McKeirnan, A.W., 2005, Large-scale psuedotachylytes and fluidized cataclasites from an ancient subduction thrust fault: Geology, 33,12, 937-940, doi: 10.1130/G21856.1.

Rybacki, E., Janssen, C., Wirth, R., Wenk, R., and Dresen, G., 2010, Low-temperature deformation in calcite veins of SAFOD core samples (San Andreas Fault) – microstructural analysis and implications of fault strength, AGU 2010 Fall Meet., San Francisco, CA, 13-17 Dec., Abstract T52B-07.

Rymer, M. J., et al., 2004,, M.J., Catchings, R. D., and Goldman, M.R., 2003, Structure of the San Andreas Fault zone as revealed by surface geologic mapping and high-resolution seismic profiling near Parkfield, California: Geophys. Res. Abs. 5, 13523.

Rymer, M. J., Tinsley, J.C. III, Treiman, J.A., Arrowsmith, J.R., Clahan, K.B., Rosinski, A.M., Bryant, W.A., Snyder, H.A., Fuis, G.S., Toke, N.A., and Bawden, G.W., 2006, Surface fault slip associated with the 2004 Parkfield, California, Earthquake: Bull. Seism. Soc. Amer., 96, 4B, S11-S27, doi: 10.1785/0120050830.

Schleicher, A.M., van der Pluijm, B.A., Solum, J.G., and Warr, L.N., 2006, The origin and significance of clay minerals on surfaces, in fractures and in veins from SAFOD borehole samples (Parkfield, California): Geophys. Res. Lett., 33, doi: 10.1029/2006GL026505.

Schleicher, A.M., Tourscher, S.N., van der Pluijm, B.A., and Warr, L.N., 2009, Constraints on mineralization, fluid-rock interaction, and mass transfer during faulting at 2-3 km depth from the SAFOD drill hole: J. Geophys. Res., 114, doi: 10.1029/2008JB006092.

Schleicher, A.M., B.A. van der Pluijm, and L.N. Warr, 2010, Nanocoatings of clay and creep of the San Andreas Fault at Parkfield, California. Geology, 38, 667-670, doi: 10.1130/G31091.1.

Scholz, C.H., 2002, The mechanics of earthquakes and faulting, 2nd ed., Cambridge Uni Press, 1-508.

Schulz, S.E., and Evans, J., 2000, Mesoscopic structure of the Punchbowl fault, southern California, and the geological and geophysical structure of active faults: J. of Struct. Geology, 22, 913–930, doi: 10.1016/S0191-8141(00)00019-5.

Sibson, R.H., 2003, Thickness of the seismic slip zone, Bull. Seism. Soc. Amer., 93, 3, 1169-1178, doi:10.1785/0120020061.

Sills, D.W., Chester, J.S., and Chester, F.M., 2009, Shape Preferred Orientation of Porphyroclasts in the Active Gouge Zones of the San Andreas Fault at SAFOD: Eos (Transactions, Amer. Geophys. Union), 90, 52, Fall Meeting supplement, abstract #T43A-2057.

Sills, D. W., 2010, The fabric of clasts, veins and foliations within the actively creeping zones of the San Andreas Fault at SAFOD: Implications for deformation processes, Texas A&M University, College Station, TX, 81 pp.

Sims, J.D., 1990, Geologic map of the San Andreas Fault in the Parkfield 7.5-minute Quad., Ca., U. S. Geological. Miscellaneous. Field Studies. Map, MF-2115, scale 1: 24000.

Solum, J.G., Hickman, S.H., Lockner, D.A., Moore, D.E., van der Pluijm, B.A., Schleicher, A.M., and Evans, J., 2006, Mineralogical characterization of protolith and fault rocks from the SAFOD MH: Geophys. Res. Lett., 33, doi: 10.1029/2006GL027285, doi: 10.1029/2006GL027285.

Solum, J.G., van der Pluijm, B.A., 2009, Quantification of fabrics in clay gouge from the Carboneras fault, Spain and implications for fault behavior, Tectonophysics, 475, 554-562.

Springer, S.D., Evans, J., Garver, J.I., Kirschner, D., and Janecke, S.U., 2009, Arkosic rocks from the San Andreas Fault Observatory at Depth (SAFOD) borehole, central California: Implications for the structure and tectonics of the San Andreas Fault zone: Lithosphere, 1, 206-225, doi: 10.1130/L13.1.

Tembe, S., Lockner, D.A., Solum, J.G., Morrow, C., Wong, T., and Moore, D.E., 2006, Frictional Strength of Cuttings and Core from SAFOD Drillhole Phases 1 and 2: Geophys. Res. Lett., 33, L23307, doi: 10.1029/2006GL027626.

Tembe, S., Lockner, D., and Wong, T.F., 2009, Constraints on the stress state of the San Andreas Fault with analysis based on core and cuttings from San Andreas Fault Observatory at Depth (SAFOD) drilling phases 1 and 2: J. Geophys. Res., 114, B11401, doi:10.1029/2008JB005883.

Thayer, M., and Arrowsmith, R., 2006, Geologic map of Middle Mountain, central California, scale 1:15,000, http://activetectonics.la.asu.edu/ Parkfield/structure.html.

Thurber, C., Roecker, S., Zhang, H., Baher, S., and Ellsworth, W., 2004, Fine-scale structure of the San Andreas Fault zone and location of the SAFOD target earthquakes: Geophys. Res. Lett., 31, L12S02, doi: 10.1029/2003GL019398.

Thurber, C., Zhang, H., Waldhauser, F., Hardebeck, J., Michael, A., and Eberhart-Phillips, D., 2006, Three-dimensional compressional wavespeed model, earthquake relocations, and focal mechanisms for the Parkfield, California, region: Bulletin of Seismological Society of America, 96, S38-S49, doi: 10.1785/0120050825.

Thurber, C., Roecker, S., Zhang, H., Bennington, N., and Peterson, D., 2010, Crustal structure and seismicity around SAFOD: A 10 year perspective, Abstract T52B-01 presented at the 2010 AGU Fall Meeting, AGU, San Francisco, CA, 13-17 Dec.

Titus, S., DeMets, C., and Tikoff, B., 2005, New slip rate estimates for the creeping segment of the San Andreas Fault, California: Geology, 33, 205–208, doi: 10.1130/G21107.1.

Titus, S., DeMets, C., and Tikoff, B., 2006, Thirty-five-year creep rates for the creeping segment of the San Andreas Fault and the effects of the 2004 Parkfield earthquake: constraints from alignment arrays, continuous global positioning system, and creepmeters: Bull. Seism. Soc. Amer., 96, S250-S268, doi: 10.1785/0120050811.

Tobin, H. Ito, H., Behrmann, J., Hickman, S., and Kimura, G., 2007, Joint IODP_ICDP Workshop Examines Challenges of Fault Zone Drilling: Scientific Drilling, Special Issue 1., 5-16, doi: 10.2204/iodsd.s01.80.2007.

Ujiie, K., Yamaguchi, A., Kimura, G., and Toh, S., 2007, Fluidization of granular material in a subduction thrust at seismogenic depths: Earth and Planetary Science Letters 259, 307-318, doi: 10.1016/j.epsl.2007.04.049.

Unsworth, M., and Bedrosian, A., 2004, Electrical resistivity structure at the SAFOD site from magnetotelluric exploration: Geophys. Res. Lett., 31, L12S05, doi: 10.1029/2003GL019405.

Unsworth, M.J., Malin, E., Egbert, G.D., Booker, J.R., 1997, Internal structure of the San Andreas Fault at Parkfield California: Geology, 25, 359-362, doi: 10.1130/0091-7613(1997)025<0359:ISOTSA>2.3.CO;2.

Van Diggelen, E., Holdsworth, R.E., de Bresser, J.H., Spiers, C., Smith, S.A., Walker, R.J., and Bowen, L., 2010, The mircrostructural character and evolution of fault rocks from SAFOD and potential weakening mechanisms along the San Andreas Fault, AGU Fall Meeting, abstract #T52B-06.

Vannucchi, , Maltman, A., Bettelli, G., and Clennell, B., On the nature of scaly fabric and scaly clay: J. of Structural Geology, 25, 5, 673-688, doi: 10.1016/S0191-8141(02)00066-4.

Vrolijk, P., and van der Pluijm, B.A., 1999, Clay gouge: J. of Structural Geology, 21, 1039–1048, doi: 10.1016/S0191-8141(99)00103-0.

Wallace, R. E., 1990, The San Andreas Fault system, California: U.S. Geological Survey Professional Paper, 1515.

White, J.C., and Kennedy, L., Evidence for cyclic brittle-ductile deformation from San Andreas Fault Observatory at Depth (SAFOD) Phase 3 Cores, Abstract T41A-2010 presented at 2010 Fall Meet., AGU, San Francisco, CA, 13-17 Dec.

Wibberley, C.A.J., and Shimamoto, T., 2005, Earthquake slip weakening and asperities explained by thermal pressurization: Nature, 436, doi:10.1038/nature03901.

Wibberley, C.A.J., Yielding, G., and Di Toro, G., 2008, Recent advances in the understanding of fault zone structure, *in:* Wibberley, C.A.J. , Kurz, W., Imber, J., Holdsworth, R.E., and Coletinni, C., (Eds.), The internal structure of fault zones: Implications for mechanical and fluid-flow properties: Geological Society of London Special Publication, 299, 5-33.

Wiersberg, T., and Erzinger, J., 2008, Origin and spatial distribution of gas at seismogenic depths of the San Andreas Fault from drill-mud gas analysis: Applied Geochemistry, 23, 1675-1690, doi: 10.1016/j.apgeochem.2008.01.012.

Yan, Y., van der Pluijm, B., Peacor, D. R., 1997, Deformation microfabrics of clay gouge, Lewis Thrust, Canada: A case for fault weakening from clay transformation *in* Holdsworth, R.E, Strachan, R.A., Magloughlin, J.F., and Knipe, R.J., eds., The Nature and Tectonic Significance of Fault Zone Weakening, Geol. Soc. of London, Special Publication No. 186, p.

Zhang, H., and Thurber, C., 2005, Adaptive mesh seismic tomography based on tetrahedral and Voronoi diagrams: Application to Parkfield, California: J. Geophys. Res., 110, B04303, doi: 10.1029/2004JB003186.

Zoback, M.D., Hickman, S.H., and Ellsworth, W.L., 2010, Scientific Drilling Into the San Andreas Fault Zone: Eos, Transactions, American Geophysical Union, 91, 22, 197-204.

FIG. CAPTIONS

Fig. 1: SAFOD study area information: a) Location of SAFOD site in central California. The central creeping segment of the San Andreas Fault (SAF) is highlighted in gray with the locked portions of the fault shown in red. Locations of large historical ruptures including the 2004 and 1966 M 6.0 Parkfield earthquakes near SAFOD; b) Borehole geometry (not to scale) and lithologic summary for the SAFOD main borehole and the inferred locations of the Buzzard Canyon Fault (BCF) and the SAF based on cuttings analyses (Bradbury et al., 2007); c)

Approximate locations of the 2007 Phase 3 cores relative to the SAFOD main borehole (modified after Hickman et al., 2005; Zoback et al., 2010). The origin represents the position of the SAFOD borehole with the distance to the east in meters shown on the x-axis. The position in meters measured depth (m MD) of the two regions of casing deformation associated with actively slipping segments of the SAF are marked as the Southwest Deforming Zone (SDZ) and the Central Deforming Zone (CDZ) following Zoback et al. (2010). The shaded region in red represents the extent of a fault-related damage zone based on geophysical data with approximate locations of microseismicity shown in the stippled red areas and faults indicated by dashed red lines (Zoback et al.; 2010); d) The extent of the low velocity zone (LVZ) determined from borehole geophysical logs (after Jeppson et al., 2010) between ~ 3-4 km MD. A dashed red-line highlights this measured shift to lower seismic velocities and the position of this feature relative to the inferred active plate boundary (Bradbury et al., 2007; Holdsworth et al., 2010), the SDZ, and the CDZ (after Zoback et al., 2010).

Fig. 2: Schematic summary of SAFOD Phase 3 core lithology and deformation (not to scale). Sample locations and lithologic information are displayed relative to each coring run and represent an integration of our results described in Tables A1-A3. Listed core depths are in meters measured depth (m MD) based on values measured during drilling and reported in the Phase 3 Core Photo Atlas (www.earthscope.org/safod). Refer to the Supplementary Material in Zoback et al. (2010) for details concerning depth correlation methods for comparing core features to the borehole geophysical log data. The rocks associated with casing deformation and the SDZ and CDZ (Hickman et al., 2005) are highlighted in red with a dashed red line along the outer core indicating the corresponding region of low velocity or damage zone of Zoback et al. (2010). Drilling mud gas-rich zones (Weirsberg and Erzinger, 2008) are denoted with a black line along the outer core.

Fig. 3. Schematic illustration of the complex internal structure of Phase 3 core and corresponding mineralogical or elemental trends. Also refer to Fig. S5 for a summary of geochemical data. Line weight thicknesses reflect the relative quantity of each mineral constituent within a particular sample as examined through whole-rock geochemical methods (XRD and/or XRF). Greater line thickness corresponds to a greater relative abundance whereas thin lines represent present in moderate to small quantities within the sample analyzed, and dashed lines indicate a

discontinuous or localized distribution. The most notable trends include: 1) the presence of large amounts of serpentinite (lizardite ± chrysotile) and saponite within the SDZ and CDZ; 2) quartz and feldspars decrease within the SDZ and CDZ; 3) magnetite and garnet phases along with pyrite mineralization border the SDZ and CDZ and increase locally within block-in-matrix materials; and 4) Nickel-oxides and chromium-oxides show elevated concentrations in the narrow zones of the SDZ and CDZ; 5) carbonates increase within the broader shear zone including the two narrow zones of the SDZ and CDZ; and 5) palygorskite is present locally throughout much of the core (likely associated with fracture fillings) but is not within the SDZ and only present in the very base of the CDZ.

Fig. 4. Images of representative lithologies and structural features present within Phase 3 Core: a) green arkosic sequence at 3142 m with coarse feldspar fragments and volcanic lithic fragments showing small-scale offsets; b) sheared black silty shale/mudstone at 3144. 6 m with exposed fracture surface exhibiting vitreous luster and a greenish hue; c) View of reddish-brown arkosic unit parallel to axis of core; d) penetrative anastomosing fabric and cataclasite within sheared black rock at 3193.7 m (Appendix A1 Table A1). Carbonate veins and cataclasite are interlayered with black staining parallel to the foliation direction; e) shiny surfaces are common along sheets separated from the core and parallel to the plane of foliation in the sheared black rock; f) pinch-and-swell shaped clasts entrained within matrix materials forming a heterogeneous block-in-matrix structure; g) fine-grained siltstone clast with a slightly folded shape yet significantly less deformed than surrounding friable matrix; and h) sheared shaley matrix and large siltstone clasts near ~ 3311 m MD that highlight the overall trend of larger clasts exhibiting less intense deformation with fewer intraclast veins near the base of Phase 3 core.

Fig. 5. Deformation at the micro-sale in Hole E core material sampled (Fig. S2) west of the main trace of the SAF plate boundary (Figs. 1-2): a) view under cross polarizer light of carbonate alteration and clay development within this matrix supported unit and also along adjacent intergranular microfractures (see white arrow) where it appears that progressive grain elongation occurs adjacent to outer margins of the slip zone; deformation lamellae are present in quartz grains in the upper left in and middle bottom photo; grain boundary migration (gbr) features in quartz grains suggest low temperature, fluid alteration and neocrystallization and/or high strain recrystallization; larger dark quartz grain shows evidence for pressure solution (ps) that extends

into surrounding matrix; indentation, interpenetration, and truncation of grains are evidence for diffusive mass transfer processes (Blenkinsop, 2000; Rutter, 1983); b) myrmekite intergrowths and fractured feldspar in grains floating within the clayey matrix; pressure solution seams occur in several grains; c) thin-section photograph illustrates angular grains boundaries, distinct green grains with abundant magnetite, and the presence of pressure solution seams; d) At 3147.5 m MD as viewed under cross polarizer light, reactivated fractures and multi-layered cataclasite plus associated microscale fracturing are evidence for multiple episodes of slip. Note the bounding slip surface is coated with dark iron-oxides (magnetite?) and neocrystallized clay. Beyond the boundaries of the main slip surfaces, grains are intensely fractured and show additional evidence for various stages of cataclasis between fractured grains and the subsequent healing of fractures.

Fig. 6. Deformation and alteration adjacent to the SDZ of Zoback et al. (2010): a) Between 3186.7 to 3193.3 m MD, the rocks within the foliated cataclasite unit exhibit an alignment of phyllosilicates and oxides within the finer matrix materials from the meso- to micro-scale (b) and cataclasite features surrounding clasts of various lithologies and/or compacted cataclasite support fluid-like injection and brecciation processes (c); d) black staining associated with fracture system near 3192.5 m MD; e) well-developed foliation within phyllosilicate-rich gouge and rough alignment of quartz and various altered grains; note high-angle hairline fracture system dissecting foliation; f) silty-shale clast mantled with clay and attached to adjacent fragment of compacted gouge (?), forming flow patterns within the matrix; note high angle fractures coated with iron-oxides (magnetite) that dissect the foliated matrix; g) Sheared interval of black fault rock/cataclasite along the western boundary of the SDZ; h) at the micro-scale the black fault rock exhibits multiple episodes of fault slip offsetting ultracatclasite layers with several phases of mineralization related to fluid-rock interactions as evident by vein geometries and compositions (Appendix A2 Table A2) and the concentration of opaque minerals (magnetite) parallel to the foliation direction; i) slip localization within clay and serpentine-rich (lizardite ± chrysotile) gouge; a crosscutting network of veins and open fractures is also observed; j) scaly clay fabric from the core catcher at 3197.8 m MD correlates to the rocks associated with active casing deformation near ~ 3192 m MD in the borehole; k) garnet (andradite(?) see Appendix A2 Table A2) porphyroclast in fault gouge of the SDZ; l) altered lithics and calcite embedded within sheared phyllosilicate-rich matrix characterizing the fault gouge of the SDZ.

Fig. 7. Rocks associated with the SDZ zone of casing deformation as measured in the geophysical logs near ~ 3192 m MD (Zoback et al., 2010) otherwise identified as Hole G Run 2 Section 7 Phase 3 SAFOD core. Due to the geological significance of this core, no samples have been taken to date: a) sketch of the internal structure highlighting cm-scale zones of finite width with varying composition and textures; b) and c) thin-section grain mounts at 3197.0 m MD are comprised of lizardite and chrysotile (foliated clast) based on XRD analyses; calcite , quartz, and ordered interlayerd chlorite-smectite clays were also identified (Appendix A2 Table A2b); d) foliated phyllosilicate-rich fault gouge at 3197.1 m MD is comprised of quartz, plagioclase, illite, and caclite with interlayered chlorite-smectite ± chlorite ± smectite ± serpentine (Appendix A2 Table A2b); e) view of clay mantled clast in plane polarized light, note concentration of magnetite grains surrounding clast that are likely associated with serpentine minerals; and f) view in polarized light with gypsum plate inserted highlights intraclast deformation with domainal fabrics due to recrystallization processes.

Fig. 8. Deformation and alteration adjacent to and within casing deformation near 3302 m MD or the CDZ of Zoback et al. (2010): a) scaly clay fabric in the fault gouge illustrating both distributed deformation and slip localization within the discrete fracture zones near the right edge of the photo; b) development of S-C fabric in serpentinite-bearing clay gouge is highlighted; opaque stringers or grains are comprised of magnetite and appear concentrated within regions associated with altered clasts; clasts (cl) and altered clasts (acl) show development of preferred orientation through rotation in the fine matrix. View is under cross-polarizer light with gypsum plate inserted; c) altered and reworked cataclasite grain embedded within the fine foliated phyllosilicate-rich matrix support repeated episodes of brittle deformation; abundant calcite veins dissect the cataclasite; view is under cross polarizer light; d) highly rounded, clay mantled, and altered serpentinite (lizardite ± chrysotile) clast within the fault gouge; e) volcanic lithic clast (basic or basalt composition) documents variability within clast compositions and the great degree of mixing within the fault gouge; and f) photomicrograph of scaly clay fabric dissected by numerous carbonate veins.

Fig. S1. Additional images of representative lithologies and structural features present within Phase 3 Core: a) reddish-brown arkose shown in cross-sectional view in Fig. 4c at 3151 m ; b) black staining and clay alteration on open fracture surface; c) black staining (carbon rich?) along contact between fracture surface and sheared shale surface shown in b); d) finely laminated and interbedded siltstone and shales. Note carbonate veins in siltstone layers/blocks do not extend into surrounding shaley layers while shale is smeared along small-scale slip surfaces; and e) matrix of shaley layers continues to be friable with a sheared and/or shiny luster on nearly every open fracture surface.

Fig. S2. Meso-scale deformation observed in Hole E core sampled west of the main trace of the SAF plate boundary (Figs. 1-2, 4): a) Evidence for low-temperature deformation and fluid-rock interactions are indicated by white arrows within the green-arkosic unit and include highly altered feldspars, reddish-brown staining parallel to fracture surfaces, and white hairline veins Refer to Figure 4a-b); b) sheared and highly fractured black shale with distinct glassy fracture surfaces that separates the two arkosic units in Hole E (Refer to Figure 4c); c) cataclasite bands offset by younger phase of slip and cataclasite generation (Refer to Figure 4d); d) slickenlined fracture surfaces are common throughout this unit (Refer to Figure 4d).

Fig. S3. Deformation and alteration adjacent to the SDZ of Zoback et al. (2010) at the meso-scale: a) Between 3186.7 to 3193.3 m MD, the rocks within the foliated cataclasite unit exhibit an alignment of phyllosilicates and oxides within the finer matrix materials from the meso- to micro-scale (See also Fig. 6) and cataclasite features surrounding clasts of various lithologies and/or compacted cataclasite support fluid-like injection and brecciation processes (Fig. 6b); b) black staining associated with fracture system near 3192.5 m MD; c) Sheared interval of black fault rock/cataclasite along the western boundary of the SDZ (See also Fig. 6e-f); and d) scaly clay fabric from the core catcher at 3197.8 m MD (Refer also to Fig. 6g-h) correlates to the rocks associated with active casing deformation near ~ 3192 m MD in the borehole.

Fig. S4. Deformation and alteration adjacent to and within casing deformation near 3302 m MD or the CDZ of Zoback et al. (2010): a) close-up image of foliated fault core gouge with large clay mantled and partially altered clast of serpentinite (lizardite); b) close up image of the core at 3297.8 m MD showing the orientation of the fabric is generally perpendicular to the core axis (redline); note green, rounded or eye shaped clasts embedded in the finer matrix. Refer to Fig. 8 for micro-scale observations near this depth.

Fig. S5. XRF whole-rock powder geochemistry of Phase 3 core samples. Major element variations for selected oxides relative to silica and illustrated as a function of structural position across the SAFOD borehole and SAF: a) On the Pacific plate between 3100-3150 m MD, higher concentrations of Al_2O_3 and SiO_2 are associated with Salinian granitoid and arkosic sedimentary rocks; b) On the North American Plate, between 3185 - 3195 m MD, the rocks have moderate Al_2O_3 and high SiO_2 concentrations associated with sheared fine-grained sandstones, siltstones and shales associated with the Franciscan and Great Valley protolith; c) In the SDZ, MgO concentrations are high whereas SiO_2 are very low due to the presence of serpentinite and smectitic clays; d) Between the SDZ and CDZ, Al_2O_3 and CaO concentrations are generally increasing with variable amounts of SiO_2 due to the presence clay alteration and localized carbonate veins ; e) In the CDZ, MgO concentrations increase again with low SiO_2 as serpentinite and other phyllosilicates increase; and f) East of the CDZ, Al_2O_3 concentrations generally increase and SiO_2 concentrations show greater variability. XRF sample processing was completed by staff at Washington State University in the GeoAnalytical Laboratory, Pullman, Washington.

Table A1. Lithologic and structural descriptions for SAFOD Phase 3 Core.

Core Interval & Depth (m MD)	**Depth (m MD)** (ft MD)	**Lithologic Unit**	**Description**
Core Interval 1 Hole E Runs 1 Sections 1-4	**3141.42 – 3144.6** (10306.5-10316.8)	**Greenish Gray Pebbly Arkosic Sandstone** *7.5 % of total core sampled*	Dark greenish-gray pebbly medium to coarse-upper arkosic sandstone occurs from the top of Hole E Core Run 1 Section 1 to the middle of Core Run 1 Section 4. It is comprised of three subunits distinguished on the basis of grain size. From 3142.4 to approximately 3141.9 m and from 3142.8 to 3144.6 m, the matrix is a coarse to very coarse, subangular to subrounded sand. Pebbly clasts comprise 5 to 15 % of these subunits, and are subrounded to subangular, equant to slightly elongate (2:1 aspect ratio), dominantly feldspathic, and up to 2.5 cm in diameter. These clasts are mostly matrix supported in a grey-green silty sand matrix. The intervening subunit, from 3141.9 to 3142.8 m, has a similar matrix but distinctly fewer and smaller (granule size) clasts. Overall unit is massive and fines upwards and displays a slight interlocking grain texture. Coarse lenses contain subangular quartz, feldspar, and mica grains, with distinct irregularly shaped, dark reddish-brown volcanic-lithics and rare flakes of serpentinite. Thin-section analyses suggest a weak fabric of slight interlocking grain texture within the matrix suggestive of deformation and/or weak metamorphism.
Core Interval 1 Hole E Run 1 Sections 4-5	**3144.6-3145.8** (10316.8-10,320.9)	**Silty Shale and underlying Siltstone** *3.2 % of total core sampled*	A dark grayish-black siltstone extends from the middle of Core Run 1 Section 4 to nearly the bottom of Core Run 1 Section 5. Approximately 90% of this unit is comprised of mesoscopically homogeneous silt and clay size particles; the remainder consists of several subunits composed of fine to medium sands with pebbles less than 0.5 cm in diameter. One of the coarser subunits, located in the center of Section 5, is greenish-black in color and approximately 10 cm thick. The other subunit is a light olive-gray siltstone that shows faint pressure solution seams and shearing near contact with the underlying grayish-red pebbly sandstone. Clasts in the coarser subunits are subrounded and predominately feldspathic in composition. A few thin (up to mm thick), non-quartz silicate veins are present. Subunit contacts are either gradational or are associated with distinct shear zones. The siltstone spanning the bottom of Section 4 and top of Section 5 is fractured and displays a weak scaly fabric.
Core Interval 1 Hole E Run 1 Sections 6-8, Run 2 Sections 1-6	**3145.8-3152.6** (10,320.9-10,343.2)	**Grayish-Red Pebbly Sandstone** *~ 16.6 % of total core sampled*	A grayish-red to brownish-gray pebbly sandstone exists between the fault contact located near the base of Core Run 1 Section 5 and the bottom of Core 2 Section 6. The matrix is composed of coarse- to very coarse subrounded sand. Clasts are up to 3 cm in diameter, subrounded to angular, elongate with aspects ratios up to 3 to 1, and dominantly feldspathic in composition. Bedding is defined by grain size variations, alignment of elongated clasts and Liesegang-type iron-oxide staining, and is subparallel (within 20 to 30 degrees) to the core axis. Several generations of fractures and mesoscale faults crosscut this unit. The mesoscale faults consist of layers of cataclasite that are up to 0.5 cm thick. Most of the fractures and faults are reddish- to dusky-brown, presumably from the oxidation of iron.
GAP IN CORE			Within this interval is the geologic boundary between the Pacific and North American Plates (Zoback et al., 2010; Springer et al., 2010; Bradbury et al., 2007).
Core Interval 2 Hole G Core Run 1 Sec 1-6 to Core Run 2 Sec 1-3	**3186.7-3193.9** (10455.2-10478.8)	**Foliated Siltstone-Shale with Block-in-Matrix Fabric** *~ 17.5 % of the total core*	The foliated siltstone-shale cataclasite extends from the top of Hole G Core Run 1 Section 1 to the middle of Core Run 2 Section 4. The cataclastic foliation is defined by a scaly fabric in the finer-grained portions, cm-thick color banding and shape fabrics formed by elongate, irregular-shaped lenses and porphyroclasts of siltstone and fine- to very fine-grained sandstone, and serpentinite. Clasts set within this fine matrix are commonly elongated, forming irregular stringers or pinch-and-swell structures with thin cross-cutting veins trending at high angles to the long axes of the clast. These lenses and porphyroclasts contain fine-grained calcite cement and pyrite(?), with numerous thin, short carbonate and zeolite veins that often are oriented at high angles to the foliation.
Core Run 2 Hole G Sec 4-5	**3193.9-3196.4** (10478.8 - 10486.8)	**Black Fault Rock** *~ 8.5 % of the total core*	Black fine- to ultra-fine grained massive and dense sheared fault rock extends from the middle of Core Run 2 Section 4 to the top of Core Run 2 Section 7. Bounding slip surfaces with extensive calcite veining parallel to the foliation direction occur at 3193.9 and 3195.8 m. Unit is dense and rich in magnesium oxides, exhibiting slight magnetism with abundant shorter veins oblique to perpendicular to foliation of bounding shear surfaces. Numerous thin (up to mm-thick) calcite veins and small calcite-bearing mesoscale faults run parallel to oblique to the foliation direction. Near the base of the unit ~ 3195.8 m it grades into a cataclastic siltstone and shale that appears to be sheared. Split surfaces are highly reflective and some are striated.

Core Run 2 Hole G Sections 6-9	**3196.4-3198** (10,486.8-10,492.3)	**Foliated Fault Gouge (SDZ)** *~ 3.9% of the total core*	Foliated gouge from the 3192 m zone of casing deformation is associated with the Southwest Deforming Zone (SDZ) after Zoback et al. (2010) and appears near the top of Core Run 2 Section 7 and continues to the bottom of the Run 2 core catcher. The gouge is a dark grayish-black, intensely sheared fault rock that is composed of particles that, for the most part, are <10 µm in diameter (defined using a 10X hand lens). The matrix is noncohesive and displays a wavy foliation defined by pervasive microscale shears that create a penetrative, micro-scaly fabric. Split surfaces are reflective and striated. Visible clasts ranging up to several cm in diameter make up 5% or less of the volume. Clast lithologies include serpentinite, very fine-grained sandstone and siltstone, compacted clay, and altered lithics of unkown composition. Milimeter-size fragments of white (calcite?) extensional shear veins also are present. Foliations are sinuous and run approximately perpendicular to the core axis, and clasts are elongated approximately parallel to the foliation. Overall, the mesoscale structure is fairly homogeneous. The upper contact of the gouge with the bounding black cataclastic siltstone and shale is inclined and sharp. The gouge also contains a block of serpentinite, approximately 30 cm thick, which is fractured and cut by white (calcite) veins up to several mm thick that are oriented both subparallel and subperpendicular to the core axis. The upper contact of the serpentinite block with the gouge is defined by an irregular, inclined, thin zone of sheared serpentinite, whereas, the lower boundary of the serpentinite block is marked by a 4-cm-thick zone of sheared bluish-green serpentinite that displays fragmented, offset and reoriented veins. The sheared serpentinite and underlying gouge are juxtaposed along a sharp, curviplanar surface that is approximately perpendicular to the core axis.
Core Run 3 Hole G Section 1	**3198.4-3199.5** (10,493.5-10,497.2)	**Interlayered Siltstone & Mudstone/Shale with Block-in-Matrix Fabric** *~ 2.7 % of the total core*	A sheared siltstone and mudstone comprised of a thinly-bedded, dark, grayish-black shale, a grayish-black to olive-gray siltstone and very fine-grained sandstone. Bedding is approximately normal to the core axis, and is highly disrupted by offset along discrete mesoscale faults and by distributed shear of the shale. Coarser grained layers and lenses are well-cemented and cut by numerous shears and thin calcite veins that are oriented at high angles to the layering. Cataclastic shale is present at the top and base of the section. A drilling-induced highly fractured zone occurs in the middle of the section.
GAP IN CORE			
Core Interval 3 Hole G Runs 4,5,6 Core Run 4 Section 1 to the bottom of Core Run 4 Section 2	**3294.9-3296.6** (10810.0-10815.5)	**Siltstone** *~ 4 % of the total core*	A sheared siltstone and sandstone characterized by greenish-black and dark greenish-gray, thinly bedded siltstone and very fine- to medium-grained sandstone that are disrupted by offset along discrete mesoscale faults and by more distributed shearing in the finer-grained layers. The more deformed bands of sandstone and sheared siltstone are dusky-brown, producing an obvious variegation. An approximately 15-cm-thick layer of greenish-gray sandstone occurs at the base of this unit; it displays a progressive loss of grain-scale cohesion with proximity to the contact with the foliated gouge below.
Core Run 4 Section 2 to the bottom of Core Run 4 Section 5	**3296.6-3299.1** (10,815.5-10,823.9)	**Foliated Fault Gouge (CDZ)** *~ 6.2 % of the total core*	The foliated gouge associated with the 3302 m zone of casing deformation or the Central Deforming Zone (CDZ) after Zoback et al. (2010), is similar in nature to the foliated gouge near the 3192 m fault, extends from the bottom of Core Run 4 Section 2 to the bottom of Core Run 4 Section 5. The gouge is a dark grayish-black, intensely sheared fault rock that is composed of particles that, for the most part, are <10 µm in diameter (defined using a 10X hand lens). The matrix is noncohesive and displays a wavy foliation defined by pervasive microscale shears that create a penetrative, mirco-scaly fabric. Split surfaces are reflective and striated. Visible clasts ranging up to several cm in diameter make up about 5% or less of the volume. Porphyroclast lithology includes serpentinite, very fine-grained sandstone and siltstone. Millimeter-size fragments of white (calcite?) veins also are present. Foliations are approximately perpendicular to the core axis and clasts are elongated parallel to the foliation. Overall, the mesoscale structure is fairly homogeneous. The contacts with the bounding cataclastic rocks are distinct and sharp, and are probable surfaces of shear or mm-thick shear zones. Near the base of the gouge there are small blocks of serpentinite and sandstone that are up to 10 cm thick and separated by clay gouge.
Core Run 4 Section 5 to the top of	**3299.1-3301.5** (10,823.9-	**Sheared Siltstone/ Mudstone with Block-in-Matrix**	A highly sheared, dark gray to black finely laminated calcareous siltstone and mudstone unit extends from the bottom of Core Run 4 Section 5 to the top of Core Run 5 Section 2. Much of the unit is highly sheared but contains lenses or clasts of less deformed horizons. The sheared, somewhat foliated fabric plus any disrupted lithologic layering and

Core Run 5 Section 2	10831.7)	**Fabric** *~ 5.9 % of the total core*	some thin discontinuous veins are oriented at a moderately high angle to the core axis. Commonly the intrablock/clast veining does not extend into the surrounding matrix.
Core Run 5 Section 2 to the top of Core Run 5 Section 4	**3301.5 - 3303.3** (10831.7-10837.6)	**Interlayered Siltstone to Very Fine-grained Silty Sandstone with Block-in-Matrix Fabric** *~ 4.4 % of the total core*	Greenish-black to gray brown siltstone and very fine-grained massive sandstone extends from the top of Core Run 5 Section 2 to the top of Core Run 5 Section 4. The top portion of this unit contains several sharp, very dark shear surfaces with a dominant foliation inclined at ~75° to the core axis. The lower portion of this unit is mostly undeformed, very fine-grained siltstone with several distinct fractures. Locally, a meshlike network of indurated dark grey faults dip both up and down the core axis.
Core Run 5 Section 4 to the bottom of Core Run 5 Section 7	**3303.3-3305.9** (10837.6-10846.2)	**Sheared and Fractured Siltstone to Very Fine Sandstone with Block-in-Matrix Fabric** *~ 6.4 % of the total core*	Medium dark-gray to light-gray siltstone to very fine sandstone extends from the top of Core Run 5 Section 4 to the bottom of Core Run 5 Section 6 (and possibly into Section 7, which has not yet been examined in detail). This unit fines downward and is dominated by deformation features consisting of 2 to 8 cm thick gouge/shear (clay-rich?) zones, all at ~ 40° to the core axis, and numerous parallel to subparallel alternating zones of cataclasite, breccia and/or noncohesive rubble. These deformed zones are interspersed with less sheared siltstone. Within this sequence are 1 to 4 cm long subrounded clasts of finely laminated siltstone to fine sandstone of similar composition to overlying units. Some boundaries of these clasts are sheared, and a few clasts contain 1 to 2 mm wide calcite veins. Pyrite is present locally within this unit. A more deformed zone starts at about 3304.8 m and extends to the bottom of this unit. This deformed zone consists of very fine-grained dark greenish gray/black siltstone and mudstone with numerous sheared surfaces and a breccia zone containing mm-sized fragments and polished striated surfaces.
Core Run 6 Section 1 to the top of Core Run 6 Section 5	**3307.4 - 3311** (10851.0-10862.9)	**Sheared and Fractured Claystone, Mudstone and Siltstone with Block-in-Matrix Fabric** *~ 7.8 % of the total core*	A dark gray black calcareous mudstone/claystone extends from the top of Core Run 6 Section 1 to the top of Core Run 6 Section 5. This unit contains a mixture of rubble zones (caused by drilling) of sheared material exhibiting a scaly fabric, and numerous subangular matrix blocks within these sheared zones. Much of the unit consists of fractured and deformed rocks with the larger clasts appearing less-deformed relative to the overlying units. Striated surfaces are still common on smaller fragments within the sheared zones. The brecciated dark-gray siltstone/mudstone and sheared siltstone is cut by several "microbreccia" zones. The dominant shear fabric is at high angles to the core axis. Especially in the upper sections, the core is quite friable and slightly soft to the touch where it is moist and contains some clay. This unit appears to coarsen into predominately siltstone and becomes slightly more indurated toward its base, where there is a transition zone containing interspersed sheared zones in a dark-gray to greenish-black finely laminated siltstone and dark gray mudstone.
Core Run 6 Section 5 to bottom of Core Run 6 Section 6	**3311-3312.7** (10862.9-10868.5)	**Sheared Claystone and mudstone gouge** *~ 4.2 % of the total core*	Sheared, grayish black claystones and mudstones within a brecciated and foliated sheared siltstone extend from the top of Core Run 6 Section 5 to the bottom of Section 6. Two large indurated clasts with prominent calcite veining are near the top of this unit. Two fold hinges of the folded foliation are present in the central part of the unit.

Table A2. Microscale observations and whole-rock powder X-ray diffraction (XRD) results from select Phase 3 whole-rock core and powdered samples. XRD compositions are listed in order of the relative estimation of different phase proportions. The identification of phases is based on analyses of the bulk XRD patterns using X´Pert High Score software as part of the X´ Pert Pro XRD system. For phases in the shales and/or fine-grained gouges not visible at the thin-section scale, verification is required by further analyses. Within these phyllosilicate-rich materials many of the peaks may overlap, thus, mineral identifications can be challenging for phases present in only small quantities. We also used optical microscopy of cuttings (Bradbury et al., 2007) for correlation. In terms of reporting these minor to trace phases, we chose a minimum threshold score match of ~ 15. A) Samples analyzed by author at Utah State University; B) For comparative reference, samples prepared and analyzed at similar depth intervals at the U.S.G.S. Menlo Park Office by D.E. Moore (Phase 3 Core Photo Atlas v. 3-4 at http://www.earthscope.org/observatories/safod) are included.

A)

Sample Location	Geologic Featured Sampled	Meso- to Micro-scale Observations	XRD Mineralogical Composition
3142 m* [10308.4 ft] ER1S1	Lithic Arkosic Sandstone	Subangular quartz and feldspar grains show intra/inter granular fracturing; concentration and weak alignment of phyllosilicate grains within matrix; etched quartz grain boundaries and overgrowth structures, diffusion of grain boundaries, grain boundary migration; alteration of biotite to chlorite; fibrous clay matrix with crystallization and/or replacement by calcite and clay minerals	Quartz + Plagioclase (Albite & Anorthite) + Microcline + Muscovite Mica + titanium aluminosilicate ± Ankerite ± Palygorskite ± Illite ± Zeolite
3144 m [10315 ft] ER1S3	Lithic Arkosic Sandstone	Extensive intra/inter-granular microfracturing; cataclastic bands are present; slightly recrystallized; deformation lamellae and pressure solution seams occur in coarser quartz fragments; grains are subangular to subrounded; irregular mafic volcanic lithics (basalt?) suggest glass has converted to clay	Quartz + Plagioclase (Albite + Anorthoclase) + Microcline ± Ankerite ± Lizardite ± Sepiolite ± Cr-oxide
3144.6 m * [10317 ft] ER1S4	Sheared Silty Black Shale/ Mudstone	Texturally immature with abundant angular grains, increased magnetite concentration, green mineral (serpentine &/or palygorskite)	Quartz + Plagioclase (Albite) + Magnetite + Lizardite ± Palygorskite ± Illite
3146.3 m* [10322.65 ft] ER1S6	Feldspathic Arkosic Sandstone	Extensive fracturing and grain comminution/cataclasis; concentration of oxides/hydroxides along slip surfaces; calcite exhibiting deformation twinning is present in veins; pressure solution seams occur in coarse quartz fragments; all grains pervasively fractured	Quartz ± Albite ± Microcline
3146.3 m [10322.6 ft] ER1S6	Shear zone	Narrow slip surfaces (< 1mm thick) marked by opaque oxides/ hydroxides with pervasive microfracturing; alteration enhanced microcracking along feldspar cleavage planes; numerous extensional microcracks	Quartz ± Albite ± Mica ± Smectite (Nontronite?)
3147.5 m [10326.4 ft] ER1S7	Feldspathic Arkose	Extensive cataclasis, microfracturing, and microfaults with multiple offsets ~ 1-3 mm.	Quartz
3147.5 m [10326.4 ft] ER1S7	Fracture Surface Coating	Cataclasite and clay with felty mineral growth along fracture surfaces	Quartz ± Albite ± Orthoclase ± Smectite (Nontronite?) ± Palygorskite
3150.3 m* [10335.6 ft] ER2S2	Feldspathic Arkosic Sandstone	Extensive cataclasis, microfracturing, and microfaults with multiple offsets ~ 1-3 mm.	Quartz ± Albite ± Mica ± Smectite (Nontronite)
GAP IN CORE			
3187.4 m [10457.3 ft] GR1S1	Clast	Clast entrained within fine-grained phyllosilicate-rich gouge; clast contains fine to very-fine grained zones of microbreccia offset by carbonate and/or zeolite veins; opaque lined microfractures link to zones of injected cataclasite comprised of opaque	Quartz + Magnetite ± Albite ± Kaolinite ± Palygorskite ± Zeolite (Gismondine) ± Garnet (Ti-rich Andradite)

		fine-grained ground mass containing porphyroclasts of quartz and claystone	
3187.5 m* [10457.6 ft] GR1S2	Foliated Phyllosilicate-rich Matrix	Claytstone and cataclasite; Extensive microbrecciation with multiple generations of carbonate-filled to clay-rich intraclast veins that mostly predate surrounding foliated cataclasite; Fractures filled with opaque groundmass form boundaries parallel to cataclasite foliation direction and connect to multiple high-angle to perpendicular zones of injected cataclasite surrounded by opaque ground mass; several clasts are rimmed by recrystallized and/or reworked cataclasite	Quartz + Kaolinite +Magnetite + Albite ± Palygorskite ± Calcite ± Garnet (Ti-rich Andradite)
3189 m [10462.6 ft] GR1S3	Finely laminated Siltstone and Shale Clast and/or Layer	Cataclasite with opaque groundmass surrounds altered and reworked cataclasite fragments containing intraclast veins; numerous anastomosing to stylolitic opaque fractures bound multiple layers/generations of cataclasite	Quartz + Magnetite + Albite ± Palygorskite ± Calcite ± Zeolite (Gismondine) ± Lizardite ± Garnet
3190.1 m* [10466.2 ft] GR1S4	Finely laminated Siltstone and Shale Clast and/or Layer	Similar to sample 3189 m above; Extensive vein development and alteration within silttone clast	Smectite (Nontronite) + Magnetite + Albite ± Kaolinite ± Palygorskite
3191.5 m [10470.9 ft] GR2S1	Foliated Phyllosilicate-rich Matrix	Opaque pressure solution seams form weak fabric within clast; localized injection of fine-grained opaque ground mass/cataclasite.	Quartz + Calcite + Kaolinite + Albite ± Garnet (Ti-rich Andradite + Almandine) ± Palygorskite ± Carbon
3192.7 m* [10474.7A ft] GR2S2	Black Cataclasite to Ultracataclasite	Ultrafine sheared black matrix rock with quartz porphyroclasts and larger lens-shaped clasts of cataclasite with crack-seal (?) calcite veins	Quartz + Carbon + Magnetite + Palygorskite + Mica ± Illite ± Lizardite ± Cr-oxide -hydroxides ± Ni-oxide -hydroxides ± Garnet (Almandine)
3192.7 m [10474.7B ft] GR2S2	Fracture Surface Coating	Ultrafine multilayered sheared matrix with quartz porphyroclasts	Quartz + Mica + Carbon (Graphite?) ± Chrysotile ± Magnetite ± Palygorskite
3193 m [10475.7 ft] GR2S3	Black Cataclasite to Ultracataclasite	Ultrafine dark altered groundmass surrounding altered rounded to subrounded grains of similar composition; quartz porphyroclasts and isolated amygdules of unknown composition are visible	Quartz + Magnetite ± Mica ± Garnet (Almandine) ± Palygorskite
3193.9 m* [10478.7 ft] GR2S4	Foliated Cataclasite	Ultrafine alternating black to dark brown to light brown (ppl) foliated to brecciated groundmass cross cut by numerous vein cycles	Quartz + Magnetite + Albite ± Chlorite-Serpentine ± Sepiolite ± Nontronite ± Fe-Ni-oxides
3194.8 m [10481.6 ft] GR2S5	Black Cataclasite to Ultracataclasite	Similar to 3193.9 m	Quartz + Magnetite + Montmorillonite-Illite + Calcite ± Anorthite ± Titanite
3195.8 m [10484.9 ft] GR2S6	Black Cataclasite to Ultracataclasite	Ultrafine cataclasite, less foliated than similar rocks above; extensive irregular fracture geometries surrounding clasts of microbreccia and reworked foliated cataclasite	Quartz + Opal-A + Sepiolite ± Allevardite ± Zeolite (Stilbite) ± Fe-oxide
3196.28 m [10486.5 ft] GR2S6	Black Cataclasite to Ultracataclasite	No thin section available	Quartz + Montmorillonite + Albite ± Zeolite (Analcime?) ± Calcite ± Lizardite ± Saponite ± Ni-oxide-hydroxide
3197.7 m* [10491.2 ft] GR2S8	Foliated Fault Gouge (SDZ)	Fine-grained foliated matrix with sandstone, serpentinite, and garnet porphyroclasts; several porphyroclasts are mantled with opaque oxides or clays forming eye-shaped to bow-tie flow patterns suggestive of high-strain; anastomosing foliated gouge exhibits well-developed S-C fabric	Quartz + Nontronite + Montmorillonite + Corrensite + Serpentine (Lizardite + Clinochrysotile) ± Nickel-oxide-hydroxide
3197.9 m [10491.8 ft] GR2S9A	Foliated Fault Gouge (SDZ)	Similar to 3197.72 m above with a greater variety of porphyroclast compositions	Quartz + Montmorillonite + Albite + Nontronite + Nickel-oxide-hydroxide + Serpentine (Lizardite) ± Zeolite (Dickite) ± Magnetite

3197.9 m [10491.8 ft] GR2S9B	Serpentinite Clast (SDZ)	Phacoidal shaped green clast entrained within foliated phyllosilicate-rich gouge matrix	Serpentine (Clinochrysotile) + Saponite ± Carbon
3198.7 m* [10494.4 ft] GR3S1	Finely Laminated Sheared Siltstone and Shale	Siltstone clast is cut by discrete carbonate veins that parallel mm-thick zones of cataclasis; serpentinite forms central vein filling of several microfractures	Quartz + Calcite ± Plagioclase (Albite + Anorthoclase) ± Serpentine (Clinochrysotile)
GAP IN CORE			
3295 m [10810.4 A ft] GR4S1	Banded Siltstone	Subangular to angular grains within silt-rich layers; detrital serpentinite grains; quartz-rich matrix; abundant aragonite	Quartz ± Plagioclase (Albite) + Magentite ± Illite ± Phillipsite
3295 m [10810.4 B ft] GR4S1	Fracture Surface Coating	Subangular to angular silty layers alternating with sheared clayey matrix; calcite and aragonite in veins	Quartz + Magnetite + Titania ± Illite ± Smectite (Nontronite) ± Cristobolite
3295.8 m* [10813.3 ft] GR4S2	Sheared Siltstone and Shale	Shear localization in clay-rich zones with altered fibrous minerals parallel to open extensional fractures; calcite microveins crosscut fine laminations	Quartz ± Plagioclase (Albite) ± Serpentine (Chrysotile) ± Illite ± Smectite (Nontronite) ± Magentite
3297.4 m [10818.2 ft] GR4S3	Foliated Fault Gouge (CDZ)	Anastomosing scaly clay fabric surrounding rounded to subrounded clasts of reworked cataclasite and serpentinite with pods or zones of a darker stained groundmass	Saponite + Serpentine (Clinochrysotile) + Quartz + Plagioclase (Anorthite) ± Carbon ± Al-Hydroxide (Gibbsite?)
3298.4 m* [10821.5 ft] GR4S4	Foliated Fault Gouge (CDZ)	Similar to SDZ samples described above	Saponite + Quartz + Serpentine (Clinochrysotile Lizardite) ± Dashkovaite? (salt)
3299.06 m [10823.7 ft] GR4S5	Sheared Siltstone and Serpentinite Clasts	Angular to subangular siltstone cut by discrete zones of cataclasite and carbonate and/or magnesite (?) veins; Serpentinite clast appears massive and highly altered containing opaque oxides and cut by opaque hairline fractures	Calcite + Quartz + Opal-A + Nontronite + Albite + Serpentine (Antigorite + Lizardite) ± Magnesite ± Cr-oxide-hydroxide
3299.9 m* [10826.4 ft] GR4S6B	Sheared Siltstone	No thin-section available	Quartz + Magnetite + Chlorite-Serpentine + Albite ± Mica (Allevardite) ± Palygorskite ± Garnet (Ti-rich Andradite) ± Serpentine (Lizardite) ± Gibbsite
3301.2 m [10830.7 ft] GR5S1	Sheared Silty Shale	Silty shale dissected by >3 mm-thick calcite vein containing at least 3 cycles of veins parallel to fracture surface that offset another series of mm- to micro veins running at moderate to high angles	Calcite + Nontronite + Albite + Illite + Palygorskite ± Magnesite ± Fe,Mg,Al oxide-hydroxides
3301.7 m* [10832.5 ft] GR5S2	Massive Siltstone	Etched grain boundaries in quartz support dissolution processes; calcite microveins and disseminated throughout fine clayey matrix; microfaults with cataclasite marked by opaque oxides/hydroxides	Quartz + Albite + Anorthite ± Calcite ± Ti-oxide
3302.6 m [10835.4 ft] GR5S3	Massive Siltstone	Similar to 3301.7 m above	Quartz ± Albite ± Mica ± Smectite (Nontronite) ± Palygorskite ± Zeolite
3303.6 m [10838.6 ft] GR5S4	Foliated Phyllosilicate-rich Matrix	Fine silty shale matrix cut by few veins, faint opaque oxide stained or white-vein filled microfractures are visible	Quartz + Mg-oxide + Albite + Illite + Zeolite ± Serpentine (Lizardite) ± Cr-oxide-hyrdoxide
3304.6 m* [10841.9 ft] GR5S5	Foliated Phyllosilicate-rich Matrix	Siltstone interlayered with massive, irregularly fractured claystone containing reduction spots; Large irregular pyrite grain is present; microfaults are visible within clay-rich clast	Quartz + Albite + Mg-oxide + Kaolinite ± Palygorskite ± Serpentine (Lizardite) ± Zeolite
3305.1 m [10843.5 ft] GR5S7	Foliated Phyllosilicate-rich Matrix	Interlayered foliated siltstone and massive claystone with faint cataclasite and microbrecciation visible	Quartz + Mg-oxide + Chlorite-Serpentine + Albite ± Illite ± Serpentine (Clinochrysotile) ± Zeolite (Laumontite)
3310.4 m* [10860.9 ft] GR6S4	Foliated Phyllosilicate-rich Matrix	Finely laminated siltstone alternating with claystone; numerous hairline fractures cut oblique to lamination direction; a few opaque stylolitic fractures run parallel to the lamination direciton	Quartz + Albite + Chlorite-Serpentine + Kaolinite ± Mica (allevardite) ± Palygorskite ± Zeolite

3311.1 m [10863.2 ft] GR6S5	Foliated Phyllosilicate-rich Matrix	Highly altered clay-rich clast dissected by numerous carbonate and zeolite(?) veins surrounded by fine-grained massive clast; reworked clasts and serpentinite form irregular fabric	Quartz + Calcite ± Anorthite ± Opal-A ± Serpentine (Lizardite) ± Carbon ± Cr-oxide-hydroxide ± Ni-oxide-hydroxide ± Zeolite
3312.1 m* [10866.5 ft] GR6S6	Foliated Phyllosilicate-rich Matrix	Finely laminated siltstone offset by numerous calcite-filled microfaults and cut by mm-scale calcite veins with well developed crystal structure	Quartz + Opal-A + Albite + Mg-oxide + Ti-Al-Silicate ± Kaolinite ± Lizardite ± Calcite ± Zeolite

*Indicates corresponding X-ray florescence sample listed in Table 3.

B)

Sample Location	Geologic Feature Sampled	XRD Mineralogical Composition
3190.6 m [10468 ft] GR1S5	Foliated Siltstone-Shale Cataclasite	Quartz + Plagioclse (Albite) ± mixed layer clays (I/S?) ± Calcite (?) ± Chlorite
3192.3 m [10473.5 ft] GR2S2	Foliated Siltstone-Shale Cataclasite	Quartz + Plagioclse (Albite) + Illite (phengite) + Calcite + Chlorite ± mixed layer clays (I/S?)
3196.5 m [10487.1 ft] GR2S7	Foliated Fault Gouge (SDZ)	Quartz + Plagioclse (Albite) + Calcite ± Serpentine ± Chlorite-Smectite (Corrensite?)
3196.9 m [10488.8 ft] GR2S7	Sheared Serpentine-bearing Fault Gouge (SDZ)	Serpentine (Lizardite ± Chrysotile) + Quartz + Calcite + Chlorite-Smectite (Corrensite?)
3197.2 m [10489.4 ft] GR2S7	Foliated Fault Gouge (SDZ)	Quartz + Plagioclse (Albite) + Calcite ± Illite (phengite?) ± Chlorite-Smectite (Corrensite?) ± Serpentine?
3197.7 m [10491.3 ft] GR2S8	Serpentine Porphyroclast (SDZ)	Serpentine (Lizardite + Chrysotile)
3296.7 m [10815.9] GR4S3	Foliated Fault Gouge (CDZ)	Quartz + Calcite + Chlorite + interlayered Chlorite-Smectite (Corrensite?) clays ± Smectite ± Chlorite ± Serpentine
3297.1 m [10817.2] GR4S3	Foliated Fault Gouge (CDZ)	Quartz + Calcite + Chlorite + interlayered Chlorite-Smectite (Corrensite?) clays ± Smectite ± Chlorite ± Serpentine
3301.3 m [10831.2] GR5S2	Sheared Siltstone and Mudstone	Quartz + Plagioclse (Albite) ± Illite (phengite) + Calcite + Chlorite ± mixed layer clays (I/S?)
3308.8 m [10855.7] GR6S2	Sheared and Fractured Claystone/Mudstone/Siltstone	Quartz + Plagioclse (Albite) ± Illite (phengite) + Calcite + Chlorite + mixed layer clays
3310.3 m [10860.5]* GR6S4	Sheared and Fractured Claystone/Mudstone/Siltstone	Quartz ± Plagioclse (Albite) ± Illite (phengite) + Calcite + Chlorite + mixed layer clays

Table A3. Whole-rock geochemistry of selected SAFOD Phase 3 samples: A) Unormalized Major Elements (Weight %); B) Unnormalized Trace Elements (ppm).

A)

Sample Depth	3142 m [10308.56 ft] ER1S1	3144.6 m [10317 ft] ER1S4	3146.3 m [10322.6 ft] ER1S6A	3150.3 m [10335.7 ft] ER2S2	3187.5 m [10457.6ft] GR1S2	3190.1 m [10466.2 ft] GR1S4	3192.7 m [10474.7 ft] GR2S2	3193.9 m [10478.7 ft] GR2S4	3197.72 m [10491.2 ft] GR2S8	3198.7 m [10494.4 ft] GR3S1	3295.8 m [10813.3 ft] GR4S2	3298.4 m [10821.5 ft] GR4S4	3299.9 m [10826.4 ft] GR4S6	3301.7 m [10832.5 ft] GR5S2	3304.6 m [10841.9 ft] GR5S5	3310.4 m [10860.9 ft] GR6S4	3312.1 m [10866.5 ft] GR6S6
SiO2	69.64	61.81	77.33	74.16	75.5	77.64	74.70	74.28	55.29	71.41	61.82	50.49	59.19	83.03	63.36	63.92	63.05
TiO2	0.615	1.064	0.149	0.432	0.650	0.616	0.571	0.50	0.493	0.198	0.718	0.341	0.436	0.354	0.775	0.805	0.765
Al2O3	16.22	19.03	12.57	14.43	12.94	12.35	14.59	11.97	9.98	7.14	14.28	6.95	8.01	8.90	17.92	16.46	16.46
FeO*	2.70	5.53	0.64	1.05	4.38	3.30	2.77	3.72	7.64	1.11	7.70	7.56	2.09	0.88	8.12	8.38	8.06
MnO	0.042	0.105	0.028	0.016	0.029	0.031	0.022	0.047	0.128	0.087	0.068	0.150	0.151	0.012	0.071	0.086	0.123
MgO	1.06	2.26	0.35	0.36	1.57	1.59	2.06	2.32	21.75	0.66	10.46	27.17	1.70	0.74	3.64	3.68	3.45
CaO	1.87	2.20	2.31	1.75	0.68	0.68	1.09	4.01	2.88	15.18	1.90	5.88	24.90	0.94	1.35	2.33	3.64
Na2O	3.09	3.03	3.24	3.57	1.17	0.97	0.75	1.50	1.31	1.70	1.30	1018	1.70	1.98	2.34	2.56	2.26
K2O	4.61	4.63	3.36	4.17	2.81	2.57	3.28	1.45	0.43	2.33	1.53	0.19	1.56	2.97	2.33	1.71	2.06
P2O5	0.153	0.342	0.038	0.061	0.281	0.251	0.177	0.201	0.105	0.180	0.227	0.084	0.266	0.189	0.101	0.081	0.138
Total	100.00	100.00	100.00	100.00	100.00	100.00	100.00	100.00	100.00	100.00	100.00	100.00	100.00	100.00	100.00	100.00	100.00

B)

Sample Depth	3142 m [10308.56 ft] ER1S1	3144.6 m [10317 ft] ER1S4	3146.3 m [10322.6 ft] ER1S6A	3150.3 m [10335.7 ft] ER2S2	3187.5 m [10457.6ft] GR1S2	3190.1 m [10466.2 ft] GR1S4	3192.7 m [10474.7 ft] GR2S2	3193.9 m [10478.7 ft] GR2S4	3197.72 m [10491.2 ft] GR2S8	3198.7 m [10494.4 ft] GR3S1	3295.8 m [10813.3 ft] GR4S2	3298.4 m [10821.5 ft] GR4S4	3299.9 m [10826.4 ft] GR4S6	3301.7 m [10832.5 ft] GR5S2	3304.6 m [10841.9 ft] GR5S5	3310.4 m [10860.9 ft] GR6S4	3312.1 m [10866.5 ft] GR6S6
Ni	0	0	5	0	37	20	20	21	917	9	467	1156	55	8	43	40	41
Cr	15	4	21	5	66	72	43	44	1117	17	390	1379	581	276	89	93	97
Sc	6	2	11	1	8	9	7	7	15	4	18	12	10	3	27	25	27
V	53	15	98	23	88	121	82	74	102	26	151	74	63	39	184	177	182
Ba	782	1278	590	1123	368	314	362	115	75	1595	407	76	603	1342	489	341	448
Rb	173	85	220	116	111	105	144	59	13	51	51	5	37	65	73	51	61
Sr	391	366	369	451	141	134	161	297	194	608	147	280	354	141	178	192	182
Zr	220	60	248	92	159	111	157	119	78	106	97	50	146	413	101	91	97
Y	17	7	22	15	18	22	17	18	14	11	16	11	15	16	16	17	25
Nb	15.8	3.6	19.9	13.2	14.7	14	12.9	12.3	309	4.3	5.9	3.2	4.1	5.0	5	3.5	4.2
Ga	20	12	28	17	19	17	19	16	9	5	18	7	7	8	19	16	16
Cu	12	2	26	2	29	34	15	20	36	8	48	27	13	5	86	67	64
Zn	71	14	143	21	95	116	87	79	75	15	148	60	64	20	115	100	94
Pb	17	18	15	17	17	10	15	14	6	6	8	6	8	10	9	7	7
La	29	16	49	26	31	34	29	29	9	13	12	7	18	21	6	10	13
Ce	59	27	91	62	58	66	53	47	20	25	22	15	29	29	18	14	24
Th	16	6	24	11	13	13	13	10	3	4	5	0	1	6	4	0	3
Nd	23	12	35	28	26	26	24	23	9	12	9	9	16	14	9	9	17
U	4	0	6	3	6	6	5	4	2	2	4	0	3	3	2	2	1

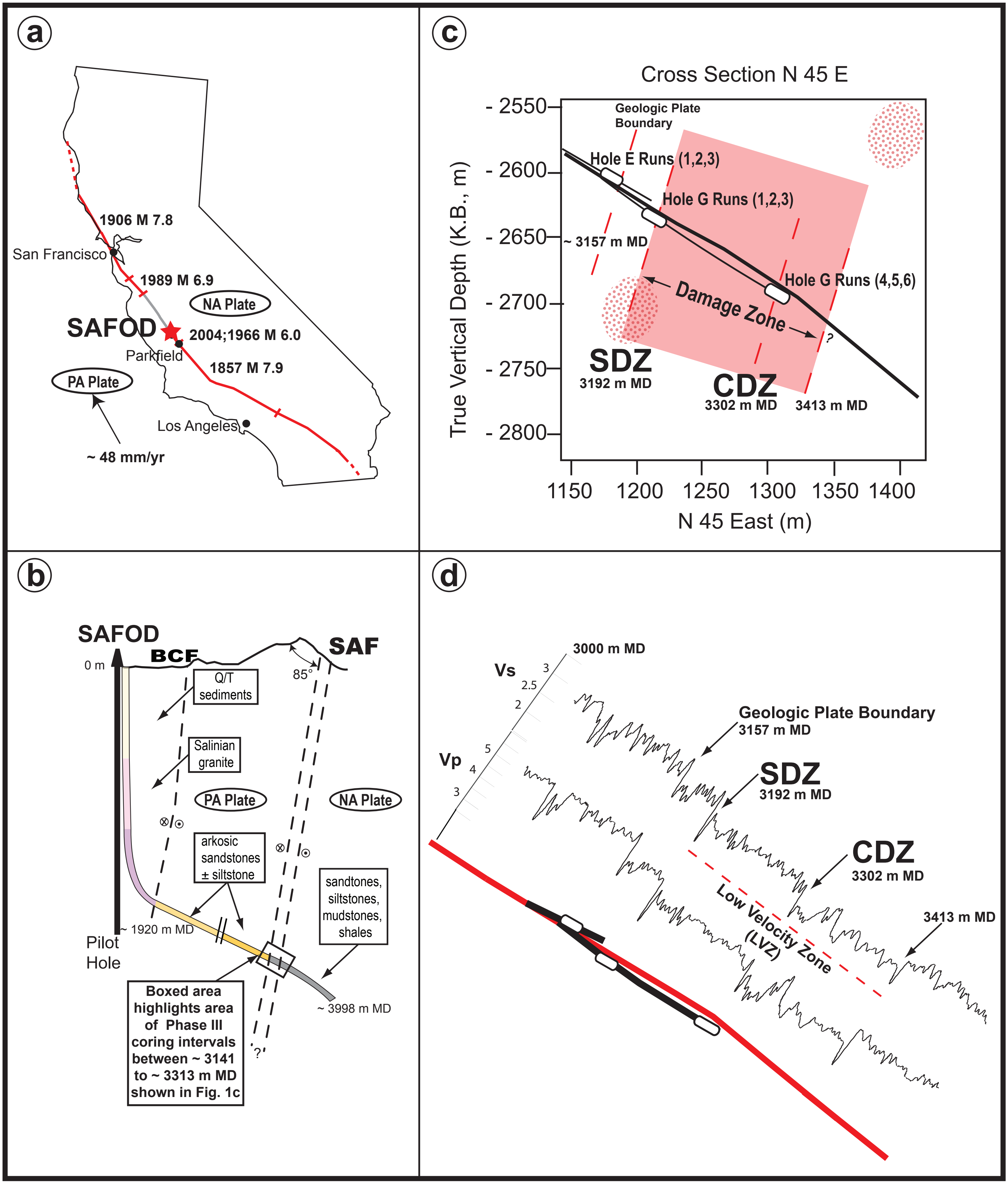
a
1906 M 7.8
San Francisco
1989 M 6.9
NA Plate
SAFOD
2004;1966 M 6.0
Parkfield
1857 M 7.9
PA Plate
Los Angeles
~ 48 mm/yr
b
SAFOD
BCF
SAF
0 m
85°
Q/T sediments
Salinian granite
PA Plate
NA Plate
arkosic sandstones ± siltstone
sandtones, siltstones, mudstones, shales
~ 1920 m MD
Pilot Hole
~ 3998 m MD
Boxed area highlights area of Phase III coring intervals between ~ 3141 to ~ 3313 m MD shown in Fig. 1c
c
Cross Section N 45 E
Geologic Plate Boundary
Hole E Runs (1,2,3)
Hole G Runs (1,2,3)
~ 3157 m MD
Hole G Runs (4,5,6)
Damage Zone
SDZ
3192 m MD
CDZ
3302 m MD
3413 m MD
True Vertical Depth (K.B., m)
- 2550
- 2600
- 2650
- 2700
- 2750
- 2800
1150
1200
1250
1300
1350
1400
N 45 East (m)
d
3000 m MD
Vs
Vp
Geologic Plate Boundary
3157 m MD
SDZ
3192 m MD
CDZ
3302 m MD
3413 m MD
Low Velocity Zone (LVZ)

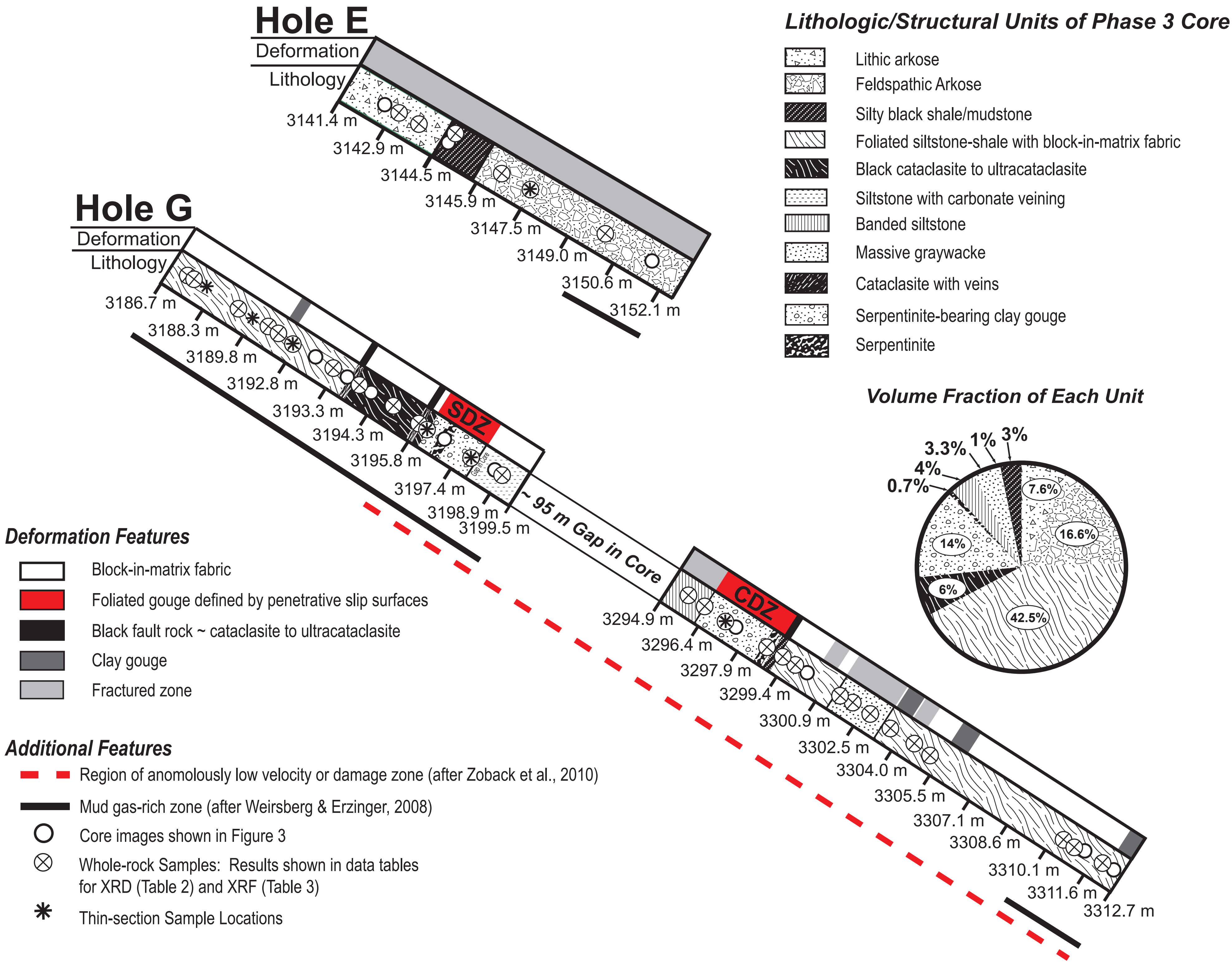
Hole E
Deformation
Lithology
3141.4 m
3142.9 m
3144.5 m
3145.9 m
3147.5 m
3149.0 m
3150.6 m
3152.1 m
Hole G
Deformation
Lithology
3186.7 m
3188.3 m
3189.8 m
3192.8 m
3193.3 m
3194.3 m
3195.8 m
3197.4 m
3198.9 m
3199.5 m
SDZ
~ 95 m Gap in Core
CDZ
3294.9 m
3296.4 m
3297.9 m
3299.4 m
3300.9 m
3302.5 m
3304.0 m
3305.5 m
3307.1 m
3308.6 m
3310.1 m
3311.6 m
3312.7 m
Lithologic/Structural Units of Phase 3 Core
Lithic arkose
Feldspathic Arkose
Silty black shale/mudstone
Foliated siltstone-shale with block-in-matrix fabric
Black cataclasite to ultracataclasite
Siltstone with carbonate veining
Banded siltstone
Massive graywacke
Cataclasite with veins
Serpentinite-bearing clay gouge
Serpentinite
Volume Fraction of Each Unit
3.3%
1%
3%
4%
0.7%
7.6%
16.6%
14%
6%
42.5%
Deformation Features
Block-in-matrix fabric
Foliated gouge defined by penetrative slip surfaces
Black fault rock ~ cataclasite to ultracataclasite
Clay gouge
Fractured zone
Additional Features
Region of anomolously low velocity or damage zone (after Zoback et al., 2010)
Mud gas-rich zone (after Weirsberg & Erzinger, 2008)
Core images shown in Figure 3
Whole-rock Samples: Results shown in data tables for XRD (Table 2) and XRF (Table 3)
Thin-section Sample Locations

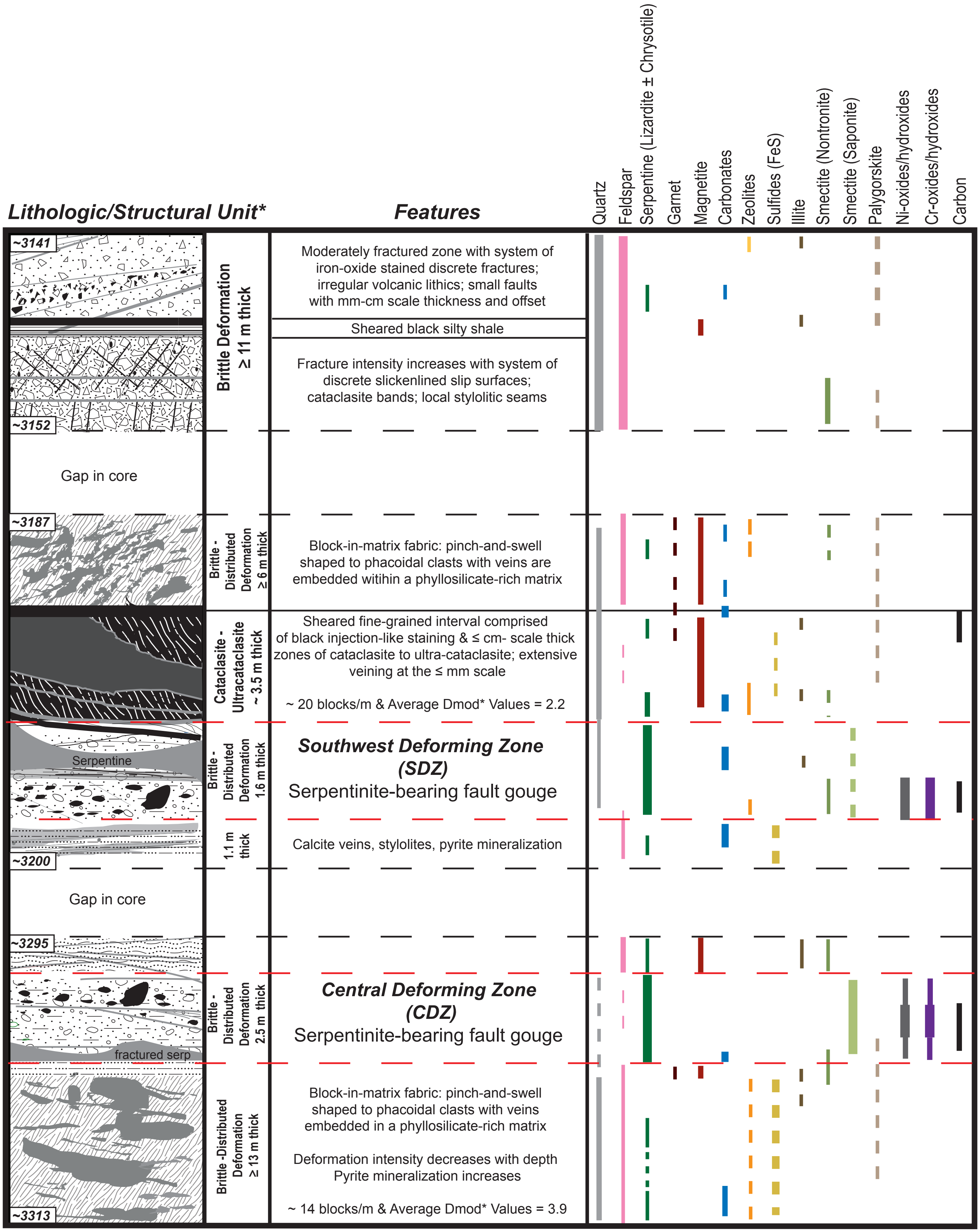

*Refer to Figure 2 for key to lithologic units and Table A1 for detailed descriptions.

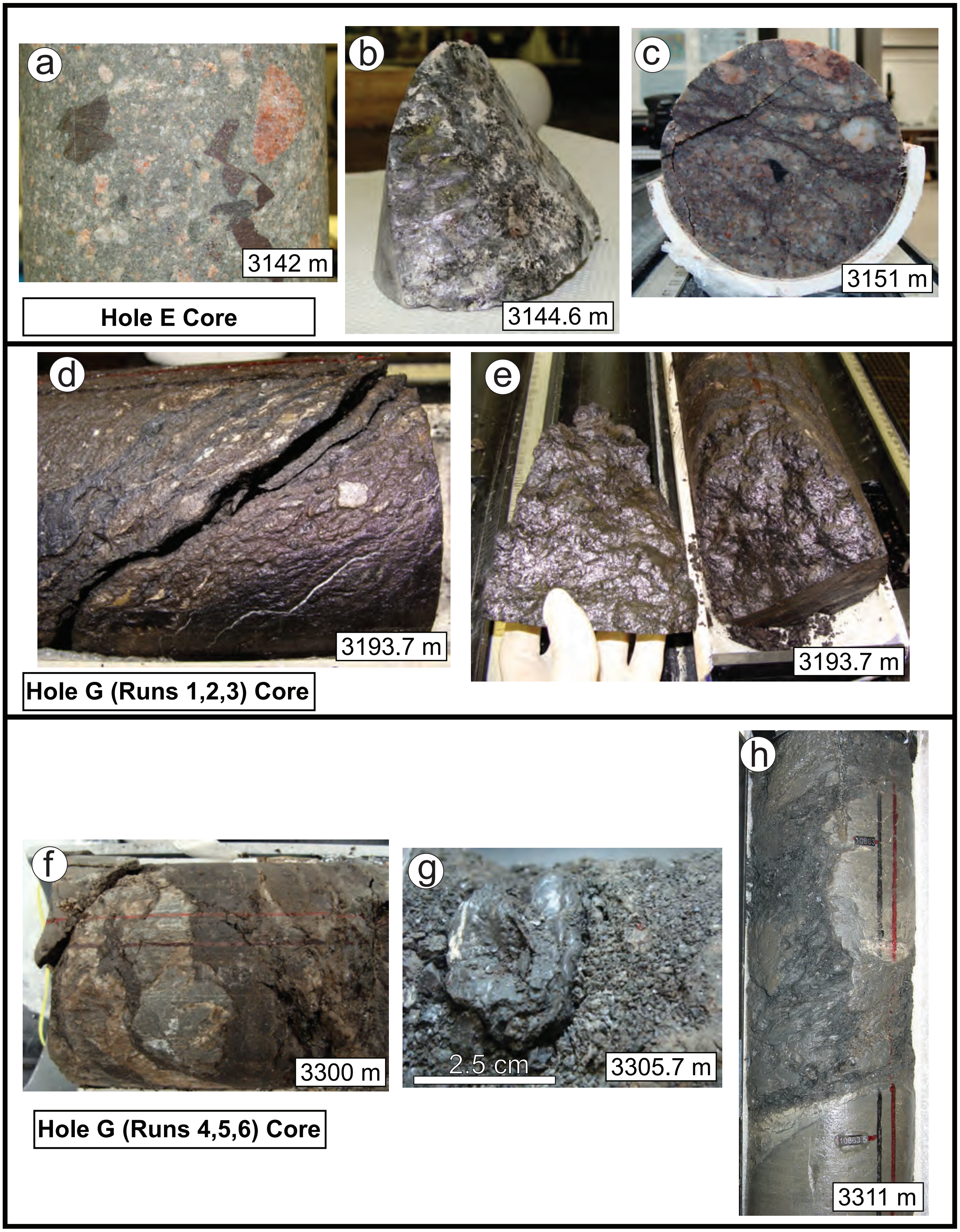
a
3142 m
Hole E Core
b
3144.6 m
c
3151 m
d
3193.7 m
Hole G (Runs 1,2,3) Core
e
3193.7 m
f
3300 m
Hole G (Runs 4,5,6) Core
g
2.5 cm
3305.7 m
h
3311 m

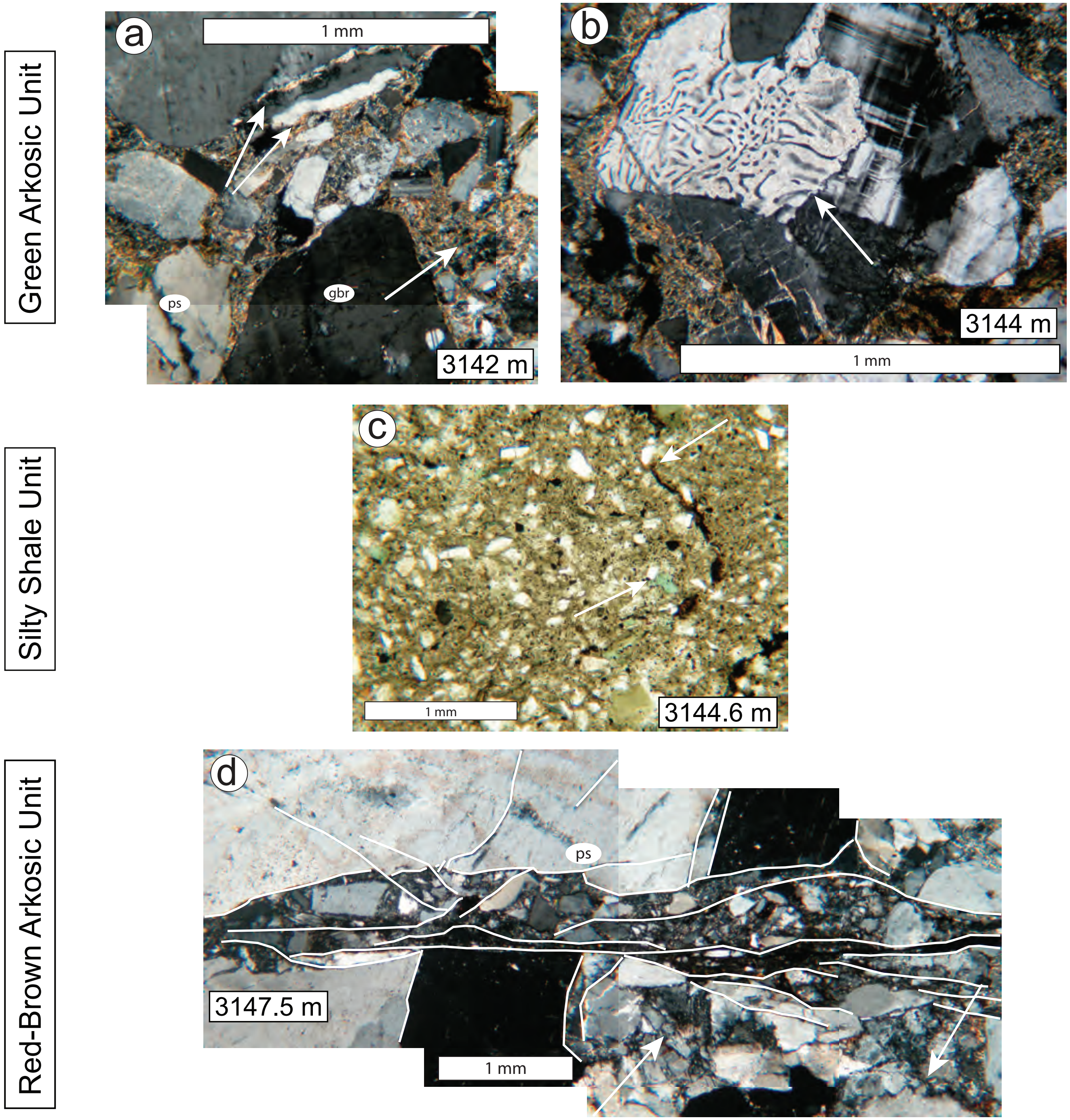
Green Arkosic Unit
a
1 mm
ps
gbr
3142 m
b
3144 m
1 mm
Silty Shale Unit
c
1 mm
3144.6 m
Red-Brown Arkosic Unit
d
ps
3147.5 m
1 mm

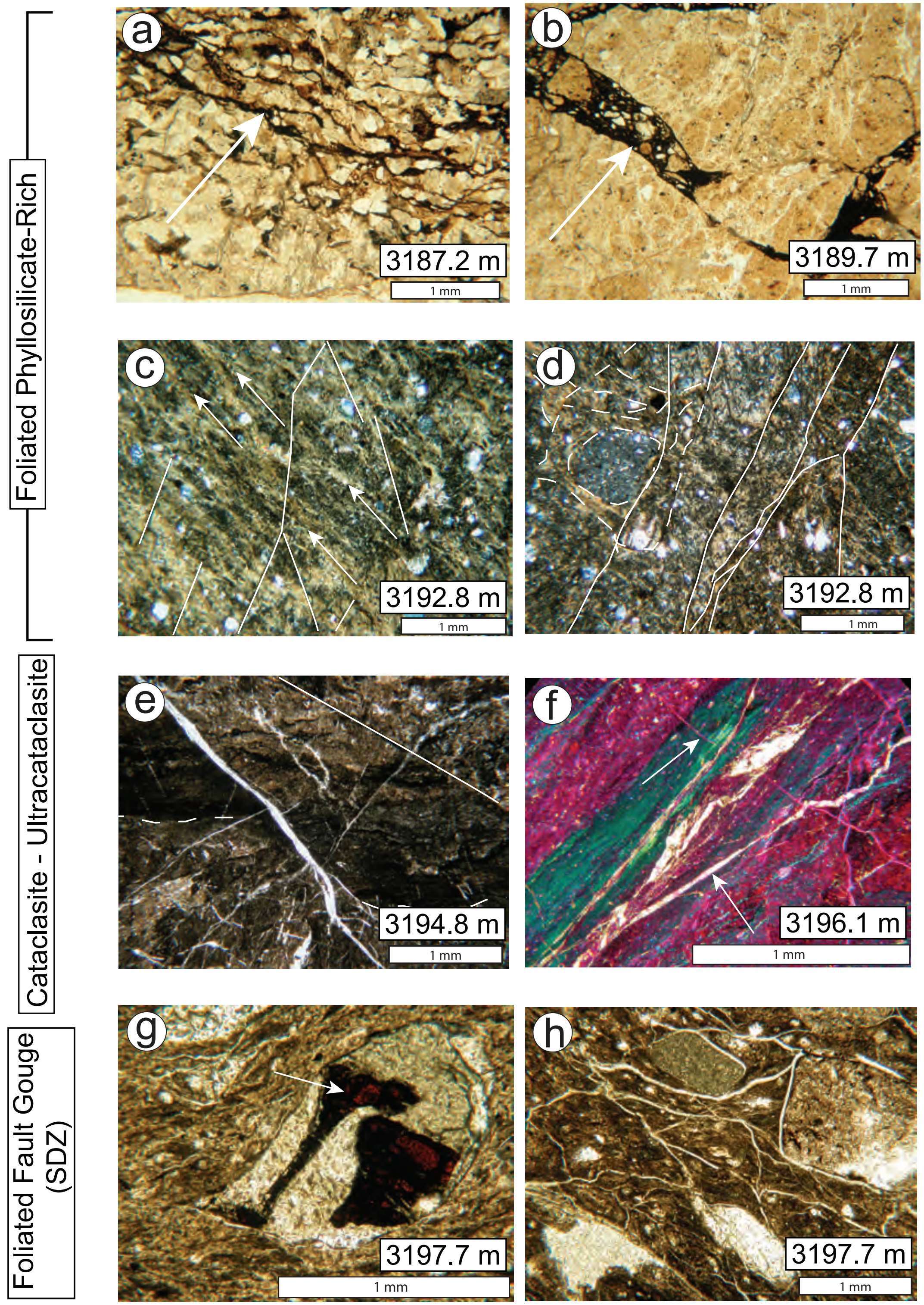

Foliated Phyllosilicate-Rich
Cataclasite - Ultracataclasite
Foliated Fault Gouge (SDZ)
a
3187.2 m
1 mm
b
3189.7 m
1 mm
c
3192.8 m
1 mm
d
3192.8 m
1 mm
e
3194.8 m
1 mm
f
3196.1 m
1 mm
g
3197.7 m
1 mm
h
3197.7 m
1 mm

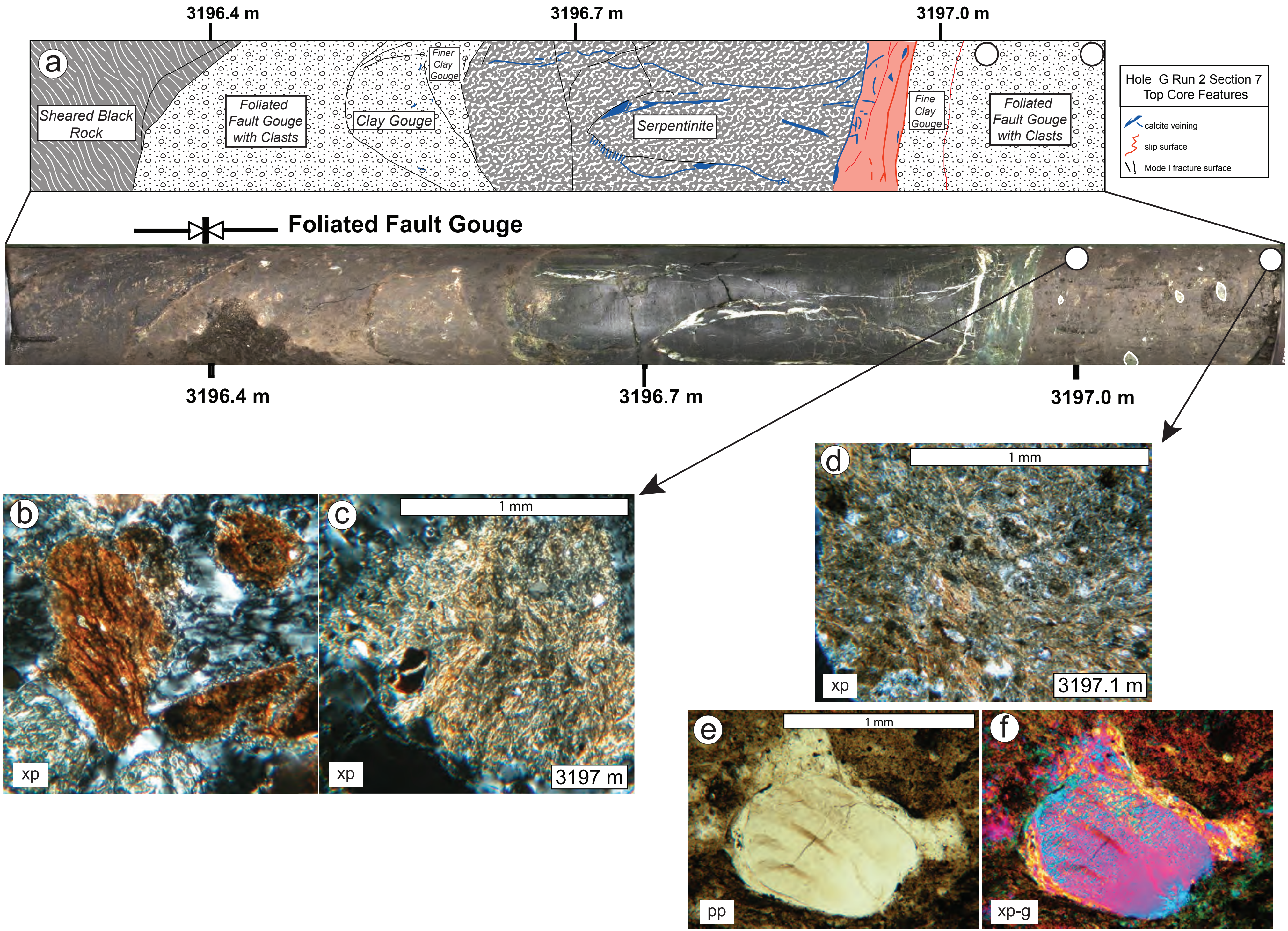

3196.4 m
3196.7 m
3197.0 m
a
Sheared Black Rock
Foliated Fault Gouge with Clasts
Clay Gouge
Finer Clay Gouge
Serpentinite
Fine Clay Gouge
Foliated Fault Gouge with Clasts
Hole G Run 2 Section 7
Top Core Features
calcite veining
slip surface
Mode I fracture surface
Foliated Fault Gouge
3196.4 m
3196.7 m
3197.0 m
b
xp
c
1 mm
xp
3197 m
d
1 mm
xp
3197.1 m
e
1 mm
pp
f
xp-g

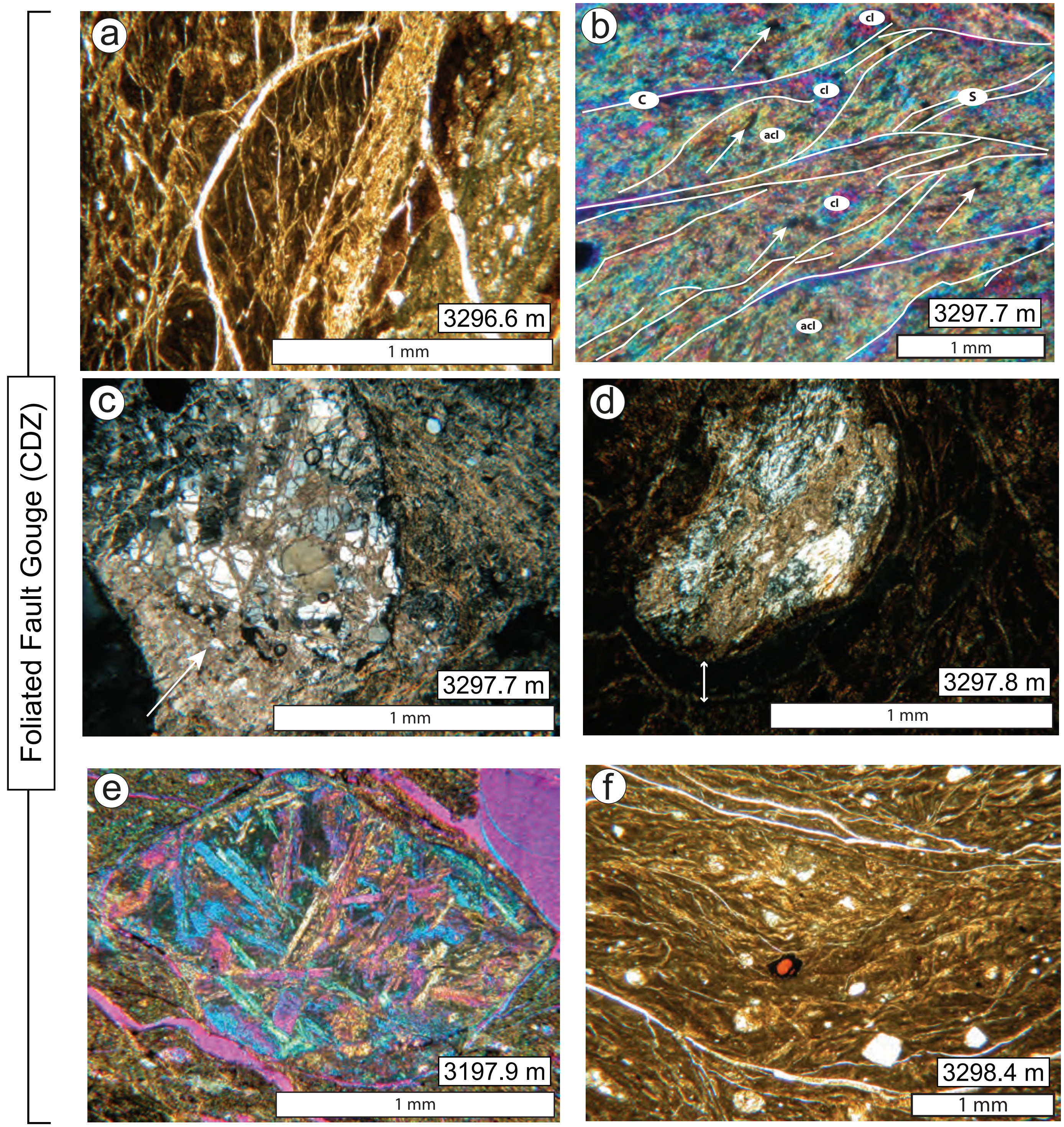

Foliated Fault Gouge (CDZ)
a
3296.6 m
1 mm
b
cl
C
cl
S
acl
cl
acl
3297.7 m
1 mm
c
3297.7 m
1 mm
d
3297.8 m
1 mm
e
3197.9 m
1 mm
f
3298.4 m
1 mm

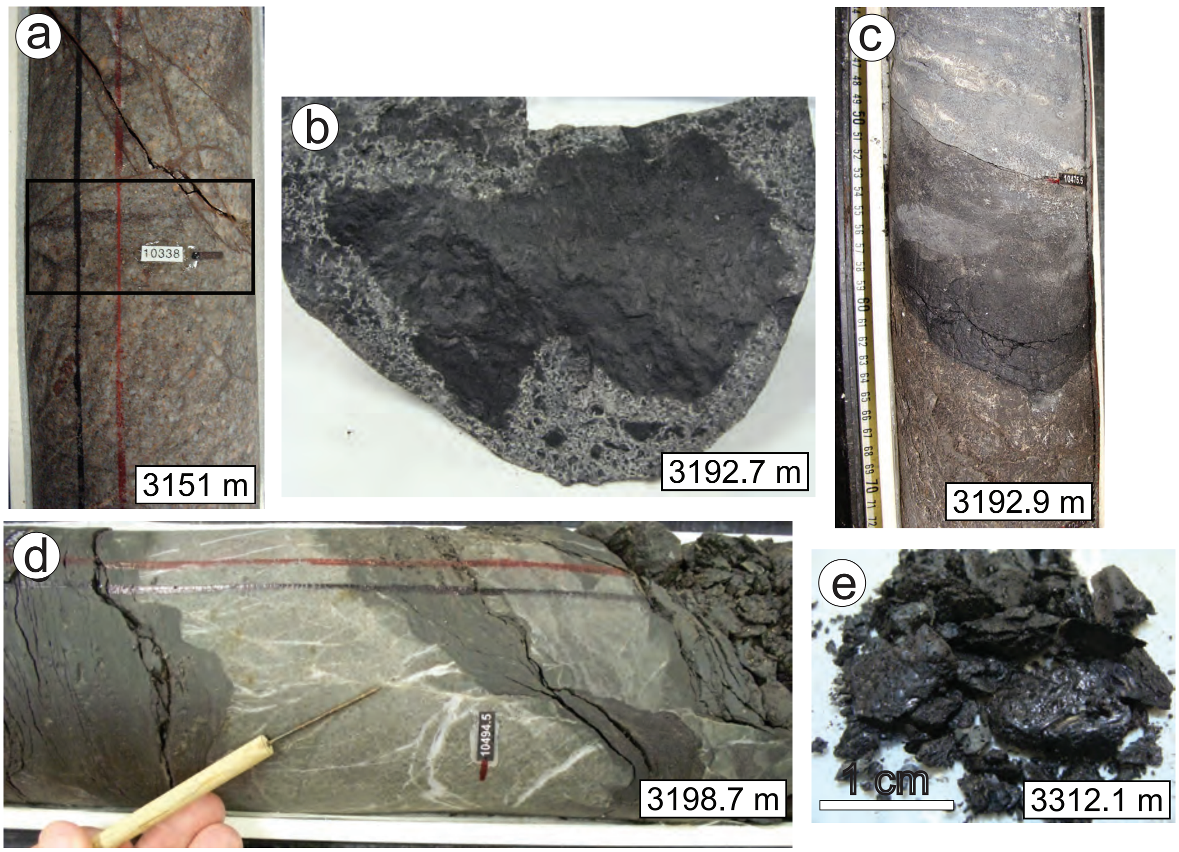
a
10338
3151 m
b
3192.7 m
c
3192.9 m
d
10494.5
3198.7 m
e
1 cm
3312.1 m

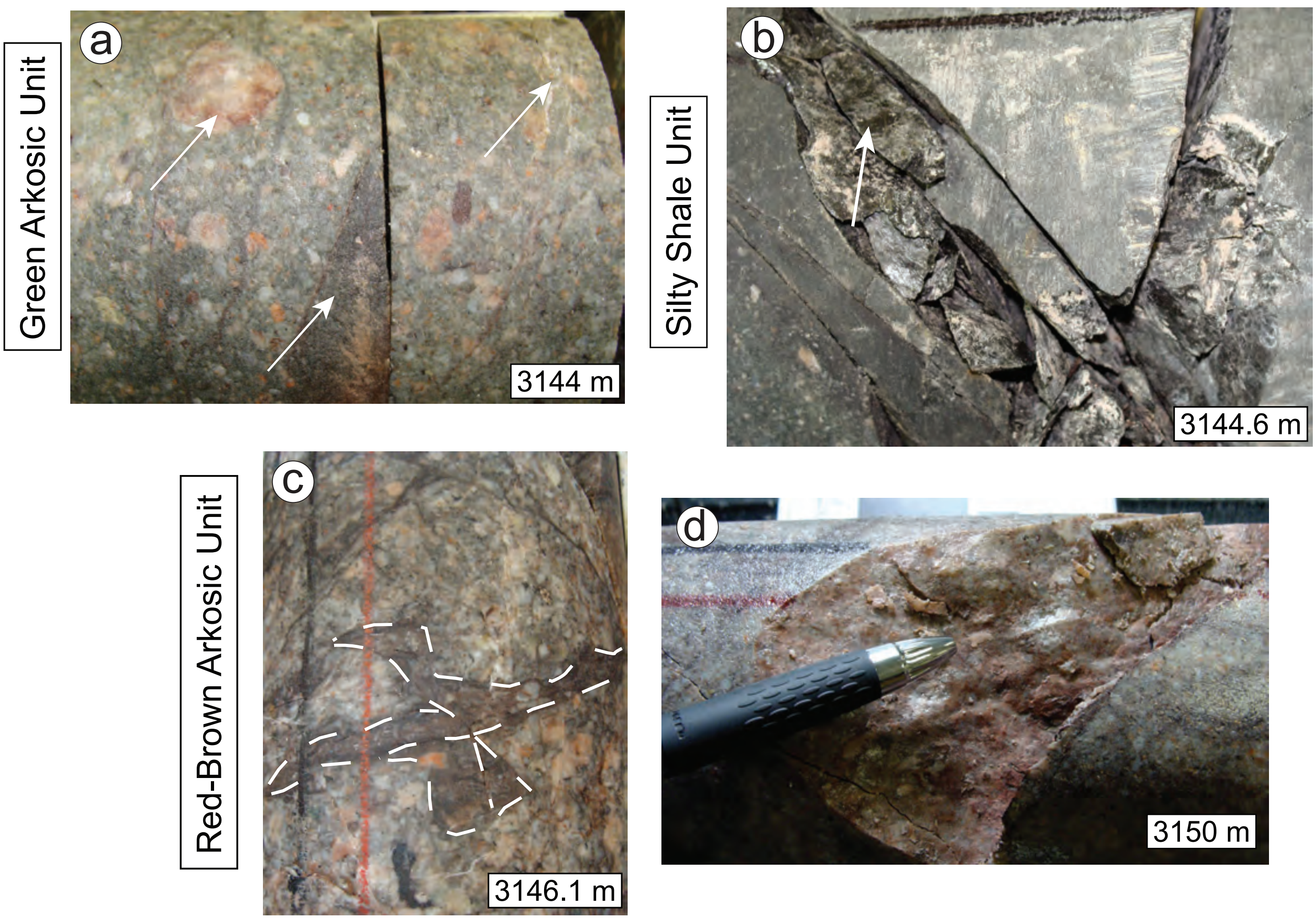
Green Arkosic Unit
a
3144 m
Silty Shale Unit
b
3144.6 m
Red-Brown Arkosic Unit
c
3146.1 m
d
3150 m

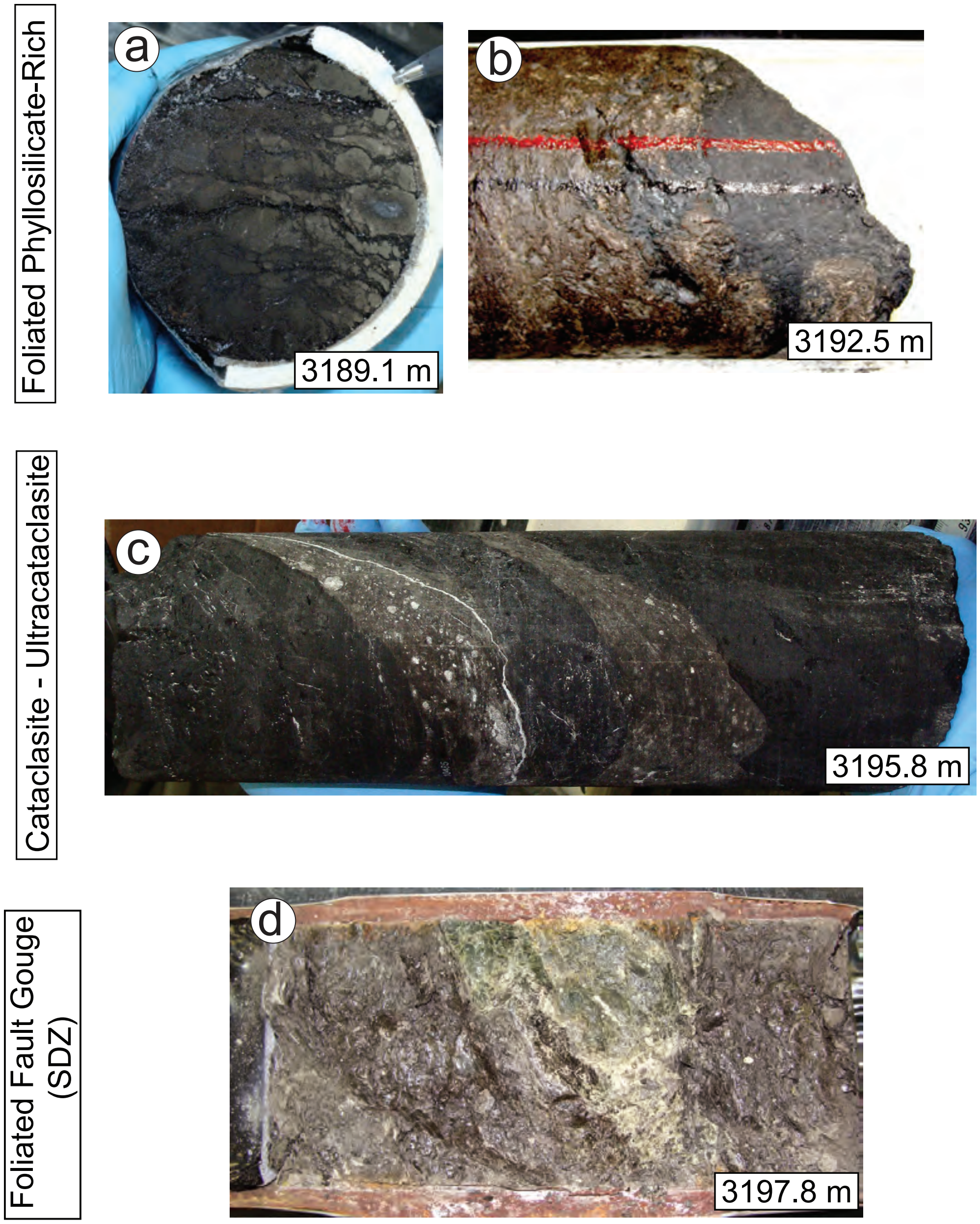
Foliated Phyllosilicate-Rich
a
3189.1 m
b
3192.5 m
Cataclasite - Ultracataclasite
c
3195.8 m
Foliated Fault Gouge (SDZ)
d
3197.8 m

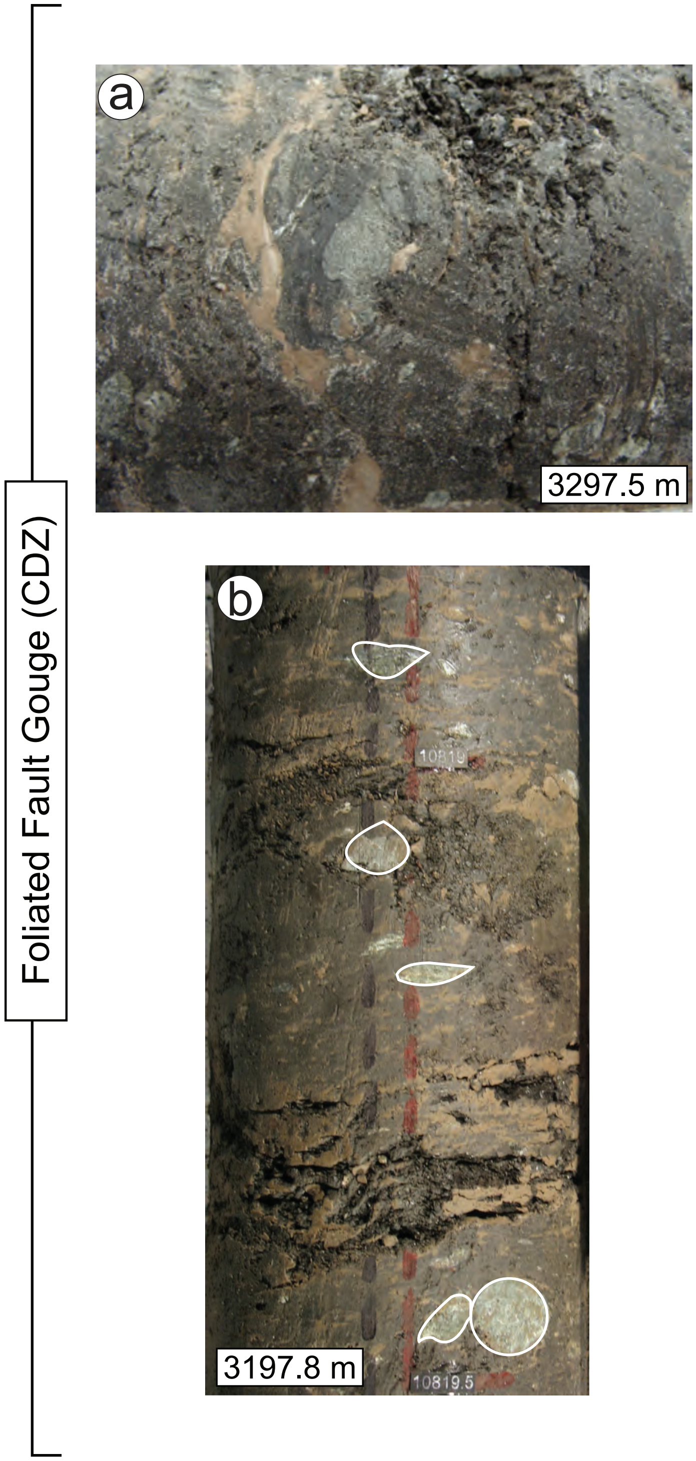
Foliated Fault Gouge (CDZ)
a
3297.5 m
b
10819
3197.8 m
10819.5

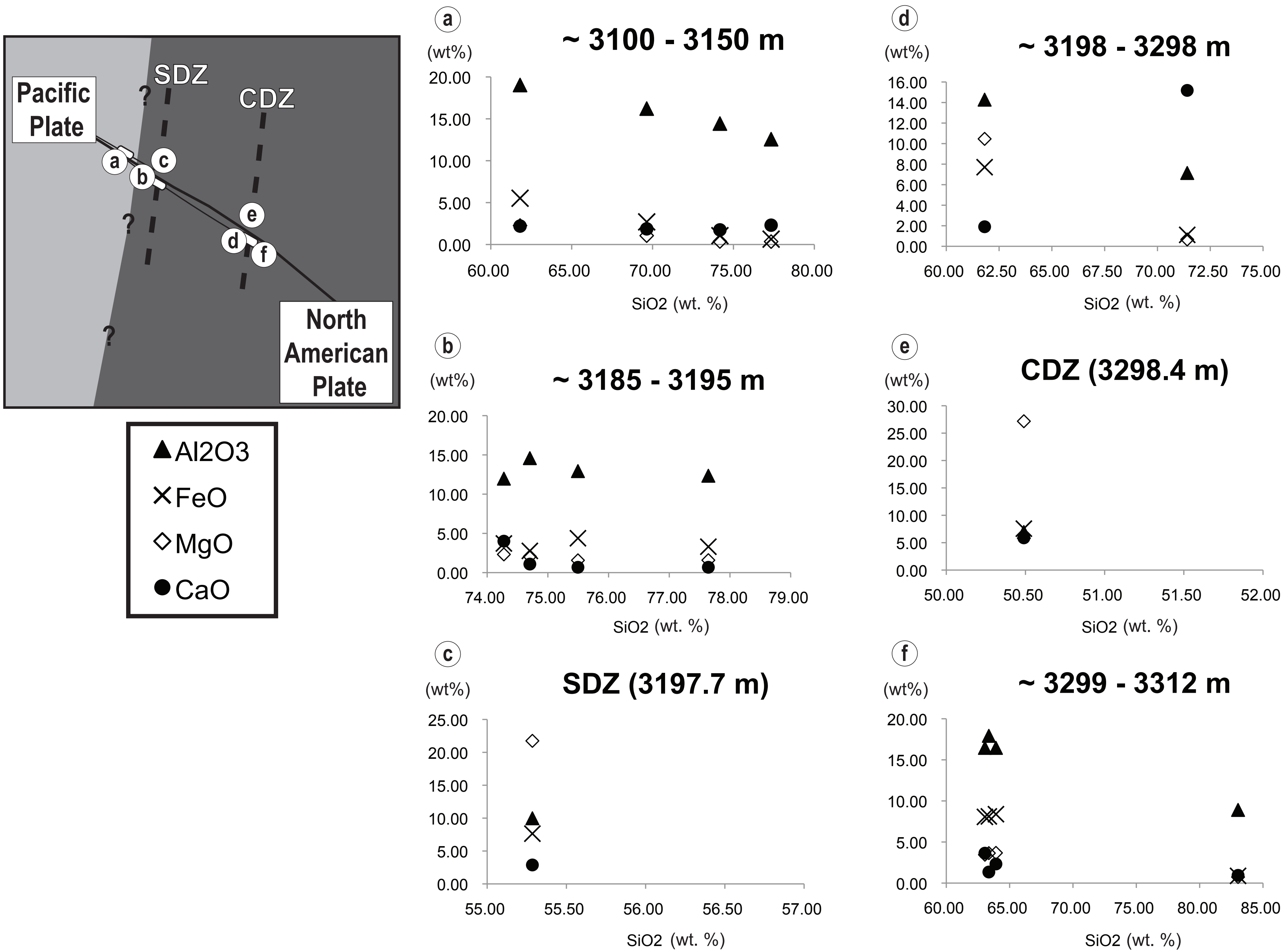

Pacific Plate
SDZ
CDZ
North American Plate
Al2O3
FeO
MgO
CaO
a
~ 3100 - 3150 m
b
~ 3185 - 3195 m
c
SDZ (3197.7 m)
d
~ 3198 - 3298 m
e
CDZ (3298.4 m)
f
~ 3299 - 3312 m
(wt%)
SiO2 (wt. %)